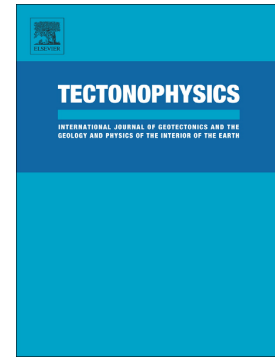# Journal Pre-proof

Shear wave velocity structure of Iranian plateau using SOLA Backus-Gilbert Rayleigh wave group velocity dispersion tomography

Saman Amiri, Mohammad Tatar, Alessia Maggi, Christophe Zaroli

Please cite this article as: S. Amiri, M. Tatar, A. Maggi, et al., Shear wave velocity structure of Iranian plateau using SOLA Backus-Gilbert Rayleigh wave group velocity dispersion tomography, *Tectonophysics* (2025), https://doi.org/10.1016/j.tecto.2025.230931

This is a PDF file of an article that has undergone enhancements after acceptance, such as the addition of a cover page and metadata, and formatting for readability, but it is not yet the definitive version of record. This version will undergo additional copyediting, typesetting and review before it is published in its final form, but we are providing this version to give early visibility of the article. Please note that, during the production process, errors may be discovered which could affect the content, and all legal disclaimers that apply to the journal pertain.

Shear wave velocity structure of Iranian plateau using SOLA Backus-Gilbert Rayleigh Wave group velocity dispersion tomography

Saman Amiri [1], Mohammad Tatar [*1], Alessia Maggi [2], Christophe Zaroli [2]

[1] International Institute of Earthquake Engineering and Seismology, Tehran, Iran,

[2] Institut Terre et Environnement de Strasbourg, UMR 7063, Université de Strasbourg, EOST/CNRS, 67084 Strasbourg cedex, France

*Corresponding author: Mohammad Tatar (mtatar@iiees.ac.ir)

ABSTRACT

We present a new shear-wave velocity (Vs) model of the Iranian Plateau using Rayleigh wave group velocity dispersion tomography. We derive the model from both seismic ambient noise and regional earthquake data using the SOLA Backus–Gilbert inversion method. The SOLA approach provides spatially variable resolution and uncertainty estimates, enabling us to produce 2D maps of Rayleigh wave group velocities whose resolutions are consistent with the lateral variations in path coverage and whose uncertainties are consistent with the resolutions. We then applied a novel homogenization strategy to equalize resolution across all periods, ensuring that local dispersion curves have uniform lateral resolution regardless of period. We applied a Bayesian Markov Chain Monte Carlo (MCMC) inversion to these homogenized local dispersion curves to construct a 3D Vs model down to 100 km depth. We interpret the models using four cross-sections that traverse key geological domains across the Iranian Plateau, revealing major lateral and vertical heterogeneities. Low Vs zones correspond to sedimentary basins and active deformation regions, while high Vs anomalies correspond to crystalline crust and upper mantle lithosphere. A prominent low-velocity anomaly beneath the Sanandaj–Sirjan Zone and southwestern Central Iran suggests asthenospheric upwelling, consistent with previous seismic and petrological studies. Our approach highlights the advantages of SOLA in quantifying resolution and uncertainty, especially in regions of sparse or heterogeneous ray coverage, and contributes a robust Vs model for seismic hazard assessment and tectonic interpretation in one of the world's most active continental collision zones.

Keywords: Rayleigh wave dispersion; SOLA Backus–Gilbert method; shear-wave velocity; resolution homogenization

1 INTRODUCTION

The convergence between the Arabian and Eurasian plates has rendered the Iranian Plateau one of the most seismically active regions on Earth. This continental collision, which began approximately 25 million years ago (e.g., Agard et al., 2011; Hatzfeld & Molnar, 2010), has produced complex structural features in the crust and upper mantle of the plateau. Over the past decades, numerous geological studies have sought to unravel the tectonic characteristics of Western Asia (e.g., Talebian & Jackson, 2004; Vernant et al., 2004; Alavi, 1994; Allen et al., 2004; Hatzfeld & Molnar, 2010; Hessami et al., 2006; Stocklin, 1968; Tatar et al., 2002).

The geological evolution of the Iranian Plateau is intricately linked to the opening and closure of the Paleo-Tethys and Neo-Tethys oceans. Following the closure of the Paleo-Tethys in the Triassic, fragments of Gondwana collided and accreted to the Turan Platform, initiating the formation of the proto-plateau. Subsequently, during the Late Triassic or Late Jurassic, the Neo-Tethys began subducting beneath Eurasia. The Arabian Plate, originally part of the Nubian Shield, began to rift away from Africa approximately 30–35 million years ago. Its eventual collision with Eurasia during the early Miocene (16–27 Ma) resulted in the closure of the Neo-Tethys, the remnants of which are still subducting beneath the Makran subduction zone (Golonka, 2004; Hatzfeld and Molnar, 2010; Hessami et al. 2001). This continued northward movement of the Arabian Plate uplifted the Zagros Mountains and shaped the modern Iranian Plateau (Stocklin, 1968; Alavi, 1994), a region marked by ongoing tectonic deformation.

The consequences of this tectonic history are expressed in variations of shear-wave velocity (Vs) across different tectonic units, including the Zagros, Sanandaj–Sirjan Zone (SSZ), Urumieh–Dokhtar Magmatic Arc (UDMA), Central Iran, and the Alborz Mountains. The tectonic framework of these units is illustrated in Fig. 1. Mentioned velocity variations are influenced by contrasts in lithospheric composition and temperature (Maggi & Priestley, 2005; Priestley & McKenzie, 2006), and in some cases, by the presence of a shallow asthenosphere beneath Central Iran (Delph et al., 2017). Additionally, major tectonic processes such as subduction and continental collision contribute to thermal anomalies and partial melting in the upper mantle, further affecting seismic wave velocity. Strike-slip faulting and complex deformation patterns also play a role in these observed variations (Goes et al., 2000; Hammond & Humphreys, 2000). Given this complexity, high-resolution and well-constrained seismic models are essential for accurately characterizing the lithospheric structure of the region.

Over recent decades, several studies have investigated the deep velocity structure and crustal thickness of the Iranian Plateau using various seismic techniques. For example, Motaghi et al. (2015) jointly inverted receiver functions and Rayleigh-wave dispersion curves along a profile from Bushehr to Sarakhs, achieving relatively good resolution in Central and Eastern Iran but failing to clearly resolve the lithosphere–asthenosphere boundary beneath the Zagros. Movaghari and Javan (2019) performed one of the recent phase-velocity tomography studies in Iran using seismic ambient noise; however, limited periods (≤ 60 s) restricted imaging to ~70 km depth, leaving the thick lithosphere beneath the Kopeh Dagh poorly resolved. Kaviani et al. (2020) conducted surface wave tomography and inversion for shear wave velocity to image the crustal and uppermost mantle structure of the entire Middle-East region using combination of seismic ambient noise and earthquakes. More recently, Irandoust et al. (2022) combined dense seismic array data with joint inversion of Rayleigh-wave group velocities and P-wave receiver functions, producing high-quality crust and upper-mantle models. In another study, Mokhtarzadeh et al. (2025) represented shear wave velocity model for western Makran.

Previous studies of surface-wave tomography in Iran have successfully imaged large-scale crustal and lithospheric structures using techniques such as LSQR damped least-squares inversion (Paige & Saunders,

1982) and the subspace inversion method (Kennett et al., 1988). However, these approaches do not provide access to the full resolution matrix or robust, spatially varying model uncertainty estimates. As a result, the degree to which the obtained velocity anomalies are reliable or comparable across different models remains unclear (Rawlinson et al., 2014). Moreover, when such models are used to derive 3D Vs structures, group velocities at different periods are inverted as if they share the same lateral resolution, even though their resolution lengths and uncertainties can differ significantly depending on path coverage. This can lead to biased results and internally inconsistent weighting of data.

We attempt to overcome these limitations in this study. We present the first shear-wave velocity model of the crust and uppermost mantle across the Iranian Plateau derived from two-dimensional Rayleigh wave tomography using the Subtractive Optimally Localized Averages (SOLA). Backus–Gilbert method adapted to seismic tomography. The SOLA method has been specifically adapted to seismic tomography to address the resolution-versus-uncertainty trade-off and enables the derivation of unbiased models with spatially variable resolution (Zaroli, 2016, 2019; Zaroli et al., 2017, Latallerie et al., 2022). SOLA not only produces full resolution and uncertainty information for tomographic models, it also constrains the models to be unbiased, and allows users direct control on the trade-off between resolution and uncertainty. We applied SOLA to a dataset of Rayleigh wave group velocity dispersion measurements, extracted from both earthquake records and seismic ambient noise cross-correlations. Using this approach, we generated a series of 2D group velocity maps for different periods, each characterized by its own spatial resolution and uncertainty, depending on path density and data coverage.

To ensure internal consistency across different periods, we introduced a homogenization step, a process uniquely enabled by the SOLA method, which equalizes the resolution at each grid point for all periods to match a reference resolution. This prevents inconsistencies that arise when group velocities with different resolutions and uncertainties are inverted together. The homogenized group velocity maps serve as the input for our subsequent shear-wave velocity inversion.

Finally, we employ a Bayesian Markov Chain Monte Carlo (MCMC) inversion to derive a 3D Vs model of the crust and uppermost mantle, using the homogenized local Rayleigh wave dispersion curves. The inversion yields shear-wave velocity profiles along with their associated 1σ uncertainties. Our resulting Vs model provides new insights into the deformation and structural complexities induced by the ongoing Arabia–Eurasia collision and enhances our understanding of lithospheric dynamics beneath the Iranian Plateau.
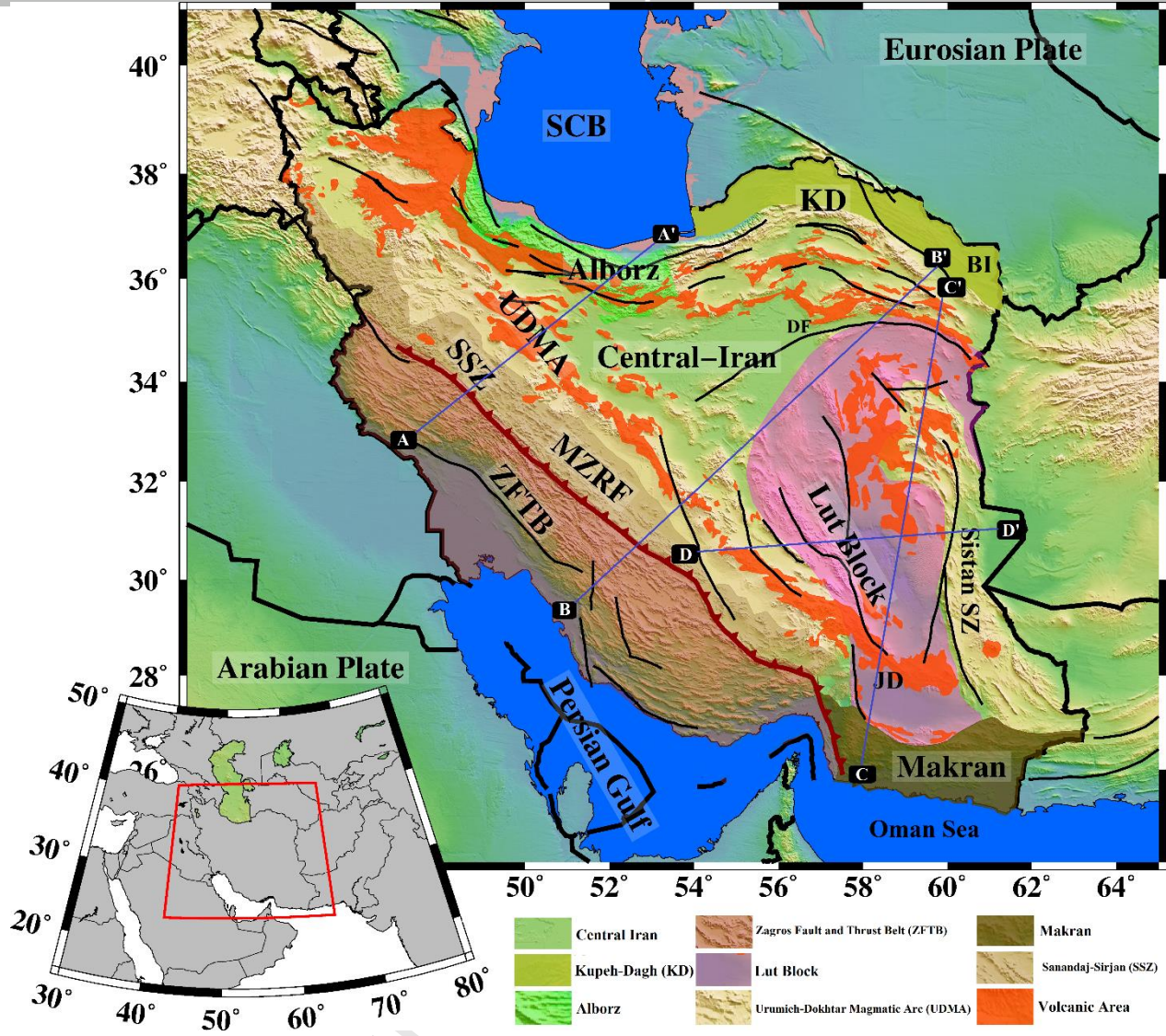
Figure 1. Topography map of the study area, showing the main seismotectonic units, and volcanic and intrusive rocks (brick orange areas). Profiles AA' and BB' both extend perpendicular to the Zagros Fold and Thrust Belt (ZFTB) and Main Zagros Reverse Fault (MZRF), crossing the Sanandaj-Sirjan Zone (SSZ), Urumieh-Dokhtar Magmatic Arc (UDMA), Central Iran, and the Kopeh-Dagh (KD). Profile CC' extends perpendicular to the Makran subduction zone, crossing the Lut Block and Jazmurian Depression (JD). Profile DD' extends perpendicular to the Sistan Suture Zone (Sistan SZ), crossing the Lut block. Locations of other important regions and faults such as South Caspian Basin (SCB), the Binalud (BI), and the Doruneh fault (DF) also indicated.

2 DATA PROCESSING

In this study, we utilized a combination of seismic ambient noise data and waveform data from local and regional earthquake events. A total of 99 broadband and mid-band stations were used, including those operated by the Iran Seismological Center (IRSC) and the International Institute of Earthquake Engineering and Seismology (IIEES) (Fig. 2). For ambient noise analysis, continuous seismic noise recorded on the vertical component of 77 broadband stations across Iran between January 2013 and December 2015 was processed to obtain empirical Green's functions. For earthquake-based analysis, vertical-component waveforms from local and regional events recorded at the same networks over the same 2013–2015 period were used. Surface waves were extracted separately from the ambient noise dataset and the earthquake waveform dataset, and both were used to measure Rayleigh wave group velocity dispersion curves along interstation paths.

2.1 Seismic ambient noise Correlation Data Processing

We followed the procedure for processing the continuous seismic noise data described in detail by Bensen et al. (2007), Lin et al. (2008), and Poli et al. (2012). First, we cut the continuous noise data into one-day data files. To diminish the amount of storage space and computational time, we decimated them to two samples per second. Then, we removed instrumental responses and linear trends and we filtered the data using a 5 to 120s period band. We used a procedure similar to that of Zigone et al. (2015) to normalize the data and minimize the effects of transients and data irregularities (for more details read Amiri et al. 2023). Then we cut the processed data into one-hour windows, cross-correlated across all available station pairs, and stacked the results over the total time period available for each pair. The correlation functions we obtained contained two-sided positive (causal) and negative (acausal) lag parts. Fig. (Supplementary) shows a series of two-sided noise correlation functions sorted by interstation distance. We averaged the two sides of each stacked correlation function to obtain one-sided symmetric correlation functions, and assessed their quality using a period-dependent signal-to-noise ratio (SNR) following the definition of Bensen et al. (2007). The SNR was calculated as the ratio of the peak amplitude within a time window surrounding the expected arrival time of the fundamental mode Rayleigh waves at a given period to the root-mean-square (RMS) amplitude of the trailing noise. The time window for the surface-wave signal was defined by arrival times corresponding to maximum (4 km/s) and minimum (2 km/s) group velocities. The peak amplitude was chosen for the signal because it represents the strongest and most coherent part of the arrival, directly reflecting the stacking stability, whereas the RMS amplitude was used for the noise as it provides a robust measure of its average energy, less sensitive to isolated spikes than a peak-based metric.

2.2 Earthquake Data Processing

We analyzed vertical recording of clear surface waves from 623 local and regional earthquakes that occurred from 2012 to 2022. These earthquakes had magnitudes greater than 4.5 and were closer than 1400 km from the stations in our networks. We decimated these recordings to 2 Hz, removed the instrument responses, and filtered between 5 and 120s period.
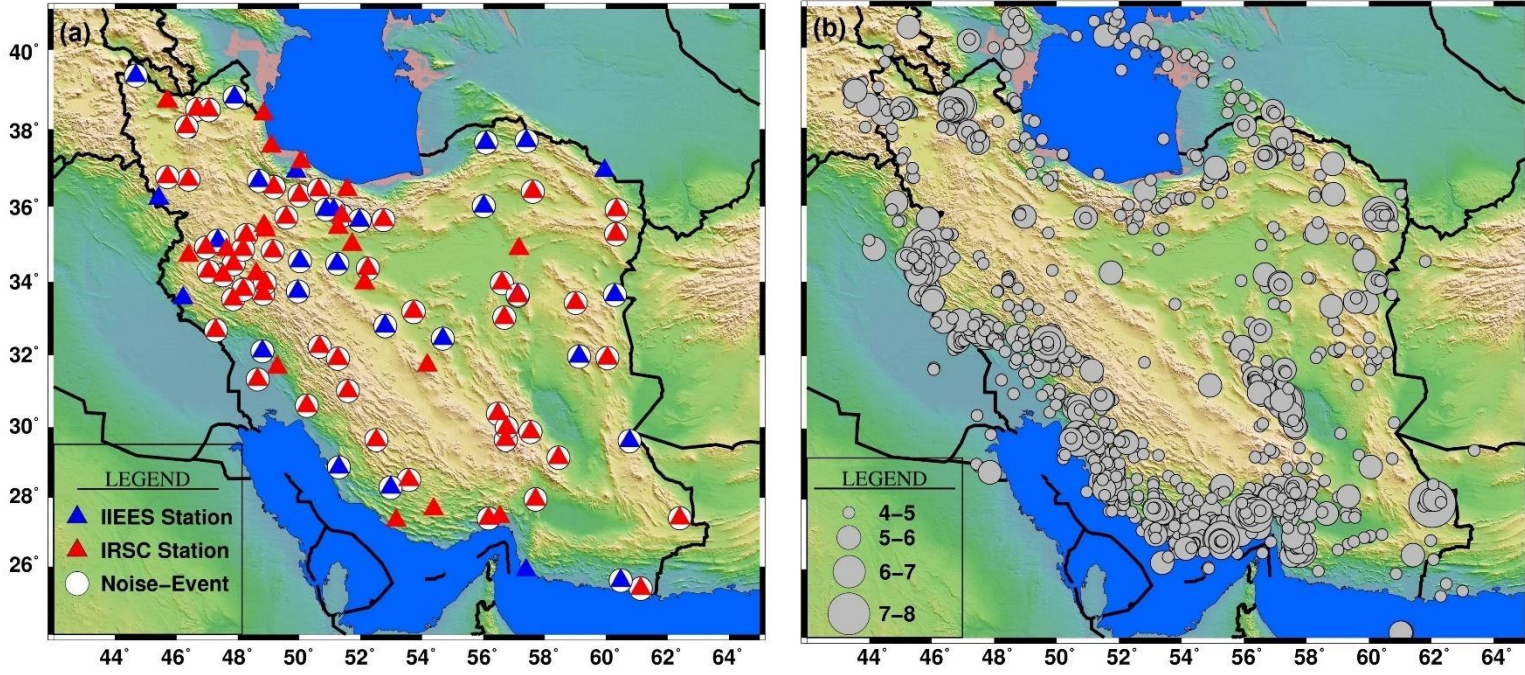
Figure 2. Locations of the used seismic stations (a) and earthquakes (b). (a) Triangles indicate stations; blue stations are from IIEES network and red ones are from IRSC. Stations surrounded by circles were used for both earthquakes and ambient noise cross-correlations while stations without circles were used only for recording earthquake data. (b) Gray circles show the distribution of earthquakes and the size of each circle denotes its M_w magnitude.

2.3 Dispersion Curves

We measured Rayleigh-wave dispersion curves from both earthquake seismograms and ambient noise correlation functions using the automated multiple filter technique of Pedersen et al. (2003) (Figure 3). For each path, we excluded records with an epicentral or inter-station distance shorter than 100 km (≈3 wavelengths) to ensure adequate sampling of the medium. Noise correlation functions with a signal-to-noise ratio below 4 were discarded. From the resulting group-velocity dispersion diagrams, we selected the period range where the maximum amplitude corresponded to the fundamental-mode Rayleigh wave, while excluding portions affected by scattered waves, multipathing, overtones, or persistent noise sources.

2.4 Data Uncertainties

Data uncertainties are a critical component in tomographic inversions because they are essential for computing accurate model uncertainties. Following Amiri et al (2023), we computed data uncertainties separately for earthquakes and noise, following two distinct approaches: one based on the maximum energy of dispersion curves for each period, applied to both seismic ambient noise and earthquake seismograms, and the other based on location uncertainties, specific to earthquake seismograms; these two uncertainties were then combined for earthquake data to define the data uncertainty for each path. After implementing the data uncertainties process, only dispersion data with SNR higher than 4 and data uncertainties below 0.35 km/s were retained for subsequent tomographic processing.

The resulting number of measurements and average group velocities at each period after considering all criteria are shown in Fig. (Supplementary) and Table 1. The resulting number of measurements and average group velocities at each period after considering all criteria are shown in Fig. (Supplementary) and Table 1. We plotted the path coverage of group velocity measurements at 30s period as a representative example in Fig. 3-a, where each path shows the measured group velocity, providing an initial view of spatial velocity variations across the region. Table 1 reveals that average group velocities increase with increasing period.

Table 1. Number of ray paths of fundamental-mode Rayleigh waves for which we measured group-velocity dispersion: average group velocity and uncertainties for measurements we retained after applying all of our selection criteria.

Period (Second)	Number of Ray Path	Average Group Velocity (km/s)	Average Uncertainties (km/s)
10	12052	2.71	0.11
20	9977	2.79	0.12
30	7395	2.89	0.14
50	3595	3.2	0.18
65	1553	3.33	0.21
85	1030	3.43	0.23

3 METHODOLOGIES

3.1 Regionalization with SOLA

We gridded the study region in steps of 0.5° in latitude and longitude and inverted our Rayleigh-wave dispersion measurements to produce group velocity maps at periods from 10 to 85s, a process called regionalization. Each model parameter m_j ($j = 1,..., M$) represents the Rayleigh wave velocity in cell j. Each d_i ($i = 1,..., N$) represents the Rayleigh wave velocity along the i_{th} source-receiver path. The sensitivity matrix G linearly relates the data to the velocities as follows:

$$d_i = \sum_{j=1}^{M} G_{ij} m_j + n_i,$$

where n_i denotes a noise term (we assume uncorrelated zero-mean Gaussian noise). The tomographic problem is ill-posed because some regions are undersampled and contradictions may arise from the noise in the data. Therefore, the linear sensitivity matrix G is not invertible and we have to seek a 'generalized' inverse matrix $G^\dagger$, such that the k_{th} parameter estimates $\tilde{m}_k$ can be written as a linear combination of the data:

$$\tilde{m}_k = \sum_{i=1}^{N} \mathbf{G}_i^{\dagger(k)} d_i = \sum_{i=1}^{N} \sum_{j=1}^{M} \mathbf{G}_i^{\dagger(k)} G_{ij} m_j + \sum_{i=1}^{N} \mathbf{G}_i^{\dagger(k)} n_i$$

Here, k refers to the kth grid cell, $G^{\dagger}(k) = (\mathbf{G}_i^{\dagger(k)})_{j=1,..,N}$ represents the kth row of the $\mathbf{G}^{\dagger}$ matrix (k may vary from 1 to M) and $\mathbf{R} = \mathbf{G}^{\dagger}\mathbf{G}$ is called the resolution matrix. For this average $\widetilde{m}_k$ to be unbiased, the averaging kernel A(k) must be constrained to satisfy the unimodular condition.

In this study, we used the SOLA (Subtractive Optimally Localised Average) variant of Backus and Gilbert's inverse theory (1967, 1968 and 1970), adapted by Zaroli (2016) for solving discrete tomographic problems. We now briefly describe the key steps of the SOLA method as we applied them to our Rayleigh-wave group-velocity tomography of Iran. For further details on the method itself, we refer the reader to Zaroli (2016), Zaroli et al. (2017), Zaroli (2019), Latallerie et al. (2022), and Amiri et al. (2023).

The aim of the Backus-Gilbert philosophy is to obtain weighted local averages over the continuous "true" model properties that are spatially localized around a given location (the center of each cell in our model parameterization). The original Backus–Gilbert scheme (1967, 1968 and 1970) consists in constructing the resolving kernel that is most strongly peaked around each model parameter location, while limiting as much as possible the noise that propagates into the model estimate (the model variance $\sigma^2_{m_{est}^{(k)}}$). The concept behind the SOLA variant lies in defining a predetermined "target form" for the resolving kernel at each point where the tomographic image computation is desired. These target resolving kernels, or target kernels, are selected so that their spatial dimensions reflect a priori estimations of the spatial resolving length at each parameter location. Instead of solely focusing on reducing the spread of individual resolving kernels, as in the original Backus–Gilbert framework, the SOLA method computes each row of Generalized inverse coefficient by minimizing an objective function that encompasses the disparity between the averaging kernel $A^{(k)}$ and a target kernel $T^{(k)}$ derived from the path distribution. Each row of the SOLA generalized inverse coefficient is individually computed by solving the following specific minimization problem:

$$\begin{cases} A_j^{(k)} = \sum_{i=1}^{N} \mathbf{G}_i^{\dagger(k)} K_{ij} \\[2mm] \sum_{j=1}^{M} V_j \left[\sum_{i=1}^{N} [\mathbf{G}_i^{\dagger(k)} K_{ij} - T_j^{(k)}]^2 + \eta^2 \, \sigma^2_{m_{est}^{(k)}} \right] = Min \\[2mm] G^{\dagger(k)} \in R^N \\[2mm] \text{Subject to} \quad \sum_{j=1}^{M} V_j \sum_{i=1}^{N} \mathbf{G}_i^{\dagger(k)} K_{ij} = 1 \end{cases} \qquad (1)$$

where K_{ij} is the sensitivity kernel (linking model space to data space). Optimization process constructs $\mathbf{G}^{\dagger(k)}$, the generalized inverse for the kth cell, using a trade-off parameter denoted as η (with a fixed value, typically set at 0.6 in this investigation) that governs the balance between resolution and uncertainties, alongside a constraint ensuring that the averaging kernel is unimodular. In the present research, the target kernels for each cell were defined as circular shapes, with radii inversely proportional to the logarithm of the path density, as previously proposed by Zaroli et al. (2017) and Latallerie et al. (2022):

$$r(\rho) = r_{max} - (r_{max} - r_{min}) \left[\frac{loglog\,(\rho - \rho)}{loglog\,(\rho max - \rho min)} \right], \qquad (2)$$

where r is the target kernel radius, constrained to lie between r_{min} and r_{max}, and ρ is the path density (sum of the columns of G) whose minimum and maximum values are ρ_{min} and ρ_{max}. The radii of the target kernels were scaled within the range of 50 km to 250 km. Path densities and the corresponding target kernel radii

for the 30s period data are depicted in Fig. 3b and c. Fig. 4 shows four target kernels and the corresponding averaging kernels produced by the SOLA inversion for different η parameters, projected onto the 0.5° grid. The size of the target kernels increases in regions of poor coverage and the shape of the averaging kernels may reveal potential smearing of information from anomalies located outside the target kernel.
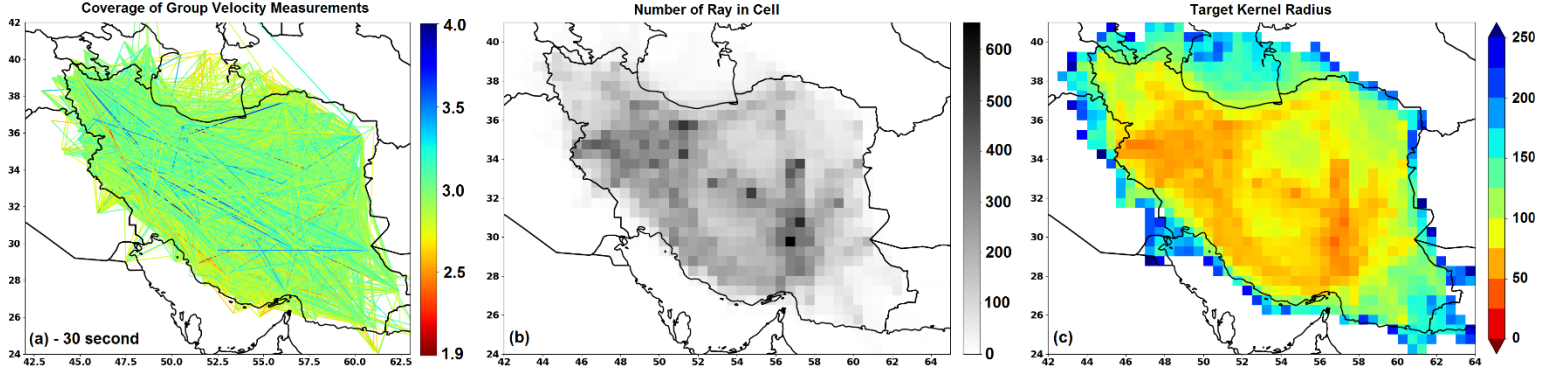

Figure 3. Path coverage/densities and SOLA target kernel radii at 30 s period. (a) Ray coverage density map for a period of 30 s. The color of rays shows the Rayleigh wave group velocity of each ray (b) The number of paths per 0.5° cell. (c) Radii of target kernels derived from the path densities using equation 2 as in Latallerie et al., (2022) and Amiri et al., (2023); cells containing no paths are masked in white.

3.2 Trade-off parameter effects on Model Uncertainties and Resolution

The SOLA trade-off parameter (η) balances model uncertainties against model resolution. As η increases, the averaging kernel exhibits larger spatial extents around the model parameter location. This expansion occurs because higher η values prioritize minimizing model uncertainties, resulting in larger averaging kernel radii relative to the target kernel radii: while model uncertainties decrease, the averaging kernels broaden, indicating poorer resolution. Conversely, lower trade-off parameters (e.g., η = 0.01) narrow the difference between the radii of averaging and target kernels. This can sometimes lead to averaging kernels with small negative components, which are theoretically insignificant and do not invalidate the results. A pronounced negative component, however, would suggest an inappropriate selection of target resolution, potentially undermining the reliability of the inversion. In our studies, any negative components are negligible and can be disregarded. Target kernel sizes in Fig. 4 expand in areas with sparse coverage, while the shape of averaging kernels suggests potential information smearing from beyond the target kernel boundaries. To streamline presentation, we summarize the averaging kernel size using the resolution length, defined as the mean of the semi-major and semi-minor axes of the ellipse containing 68% of the averaging kernel's distribution.
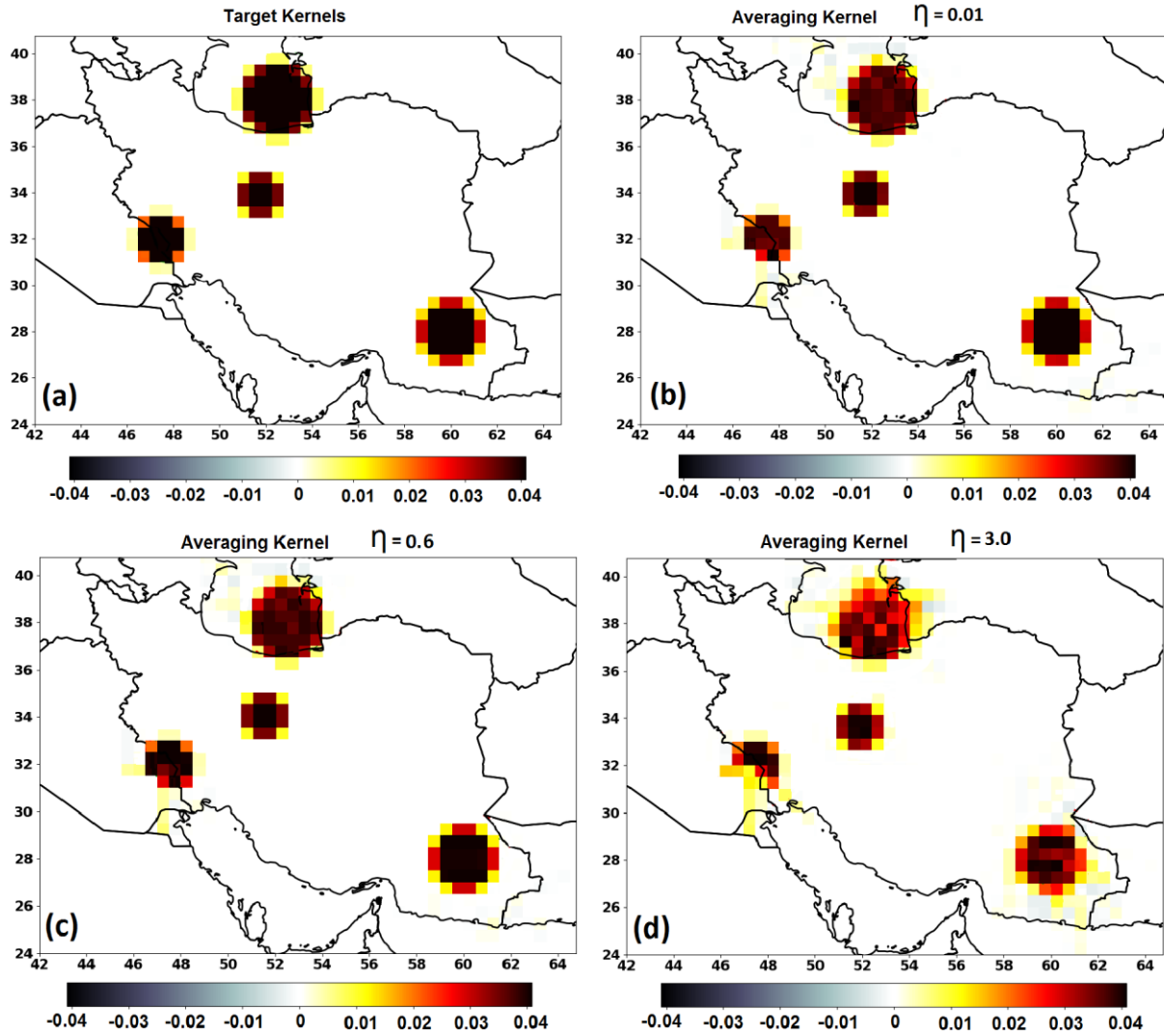
Figure 4. Target and averaging kernels for the SOLA inversion at 10 s period. (a) Circular target kernels at locations with different path densities. (b,c,d) Averaging kernels obtained after a SOLA inversion with η = 0.01, 0.6 and 3.

Fig. 5 shows an L-curve of mean resolution versus mean uncertainty for 5 values of the trade-off parameter; 3, 1, 0.6, 0.1, and 0.01. Decreasing η from 3 to 1 improves resolution greatly while increasing model uncertainties only slightly; however, decreasing η again from 0.1 to 0.01 improves resolution only slightly while increasing model uncertainties greatly. In Fig. 6 we show tomographic models, uncertainty maps, and resolution lengths obtained using three different (η) parameters (η = 3, η = 0.6, and η = 0.01). In all maps, resolution deteriorates near the model borders where the path coverage is sparse. As anticipated by Fig. 4, decreasing the trade-off parameter exacerbates model uncertainties but enhances model resolution.

Tomographic models in Fig. 5 exhibit smoother profiles and longer resolution lengths with lower uncertainties for highest value (η = 3), whereas in the lowest value (η = 0.01) result in rougher models with shorter resolution lengths and higher uncertainties. No model is inherently superior; a model with poorer resolution and lower uncertainties might suit applications requiring precise estimates of average Rayleigh wave velocity over large areas. Conversely, models with better resolution but higher uncertainties are suitable for detecting smaller anomalies expected to be sufficiently strong despite increased uncertainties. To select the trade-off parameter η, balancing resolution and uncertainty in the SOLA inversion, we opted for η = 0.6 across all maps.
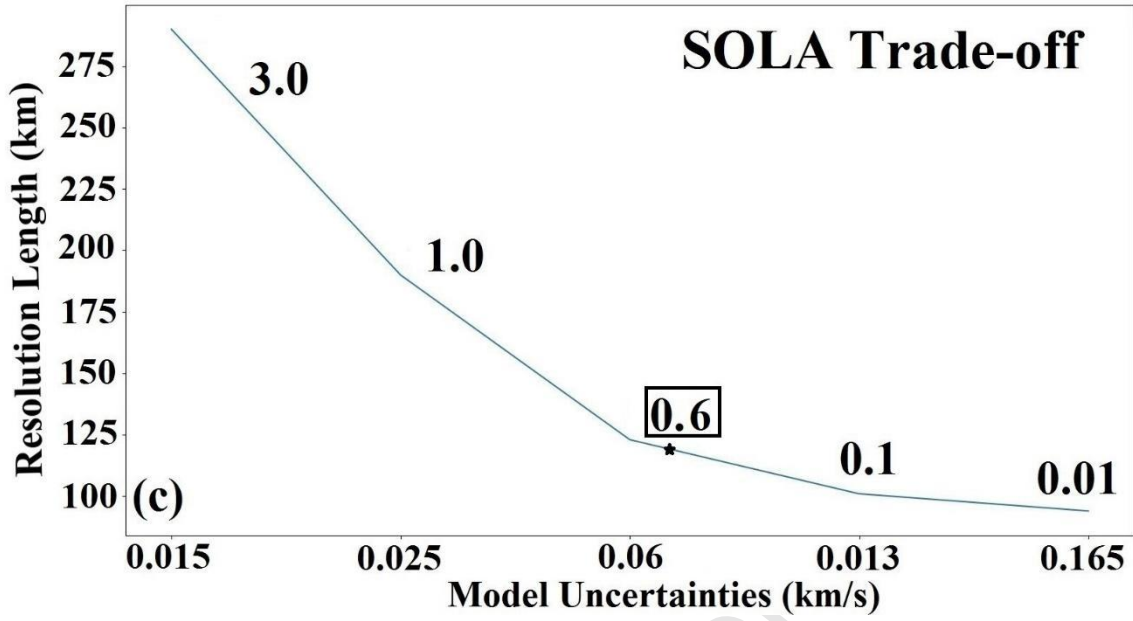
Figure 5. A trade-off between average resolution and uncertainty for the SOLA method for different values of the η for inversion of our 10s data. The number in the box shows the chosen trade-off value for the rest of this study.
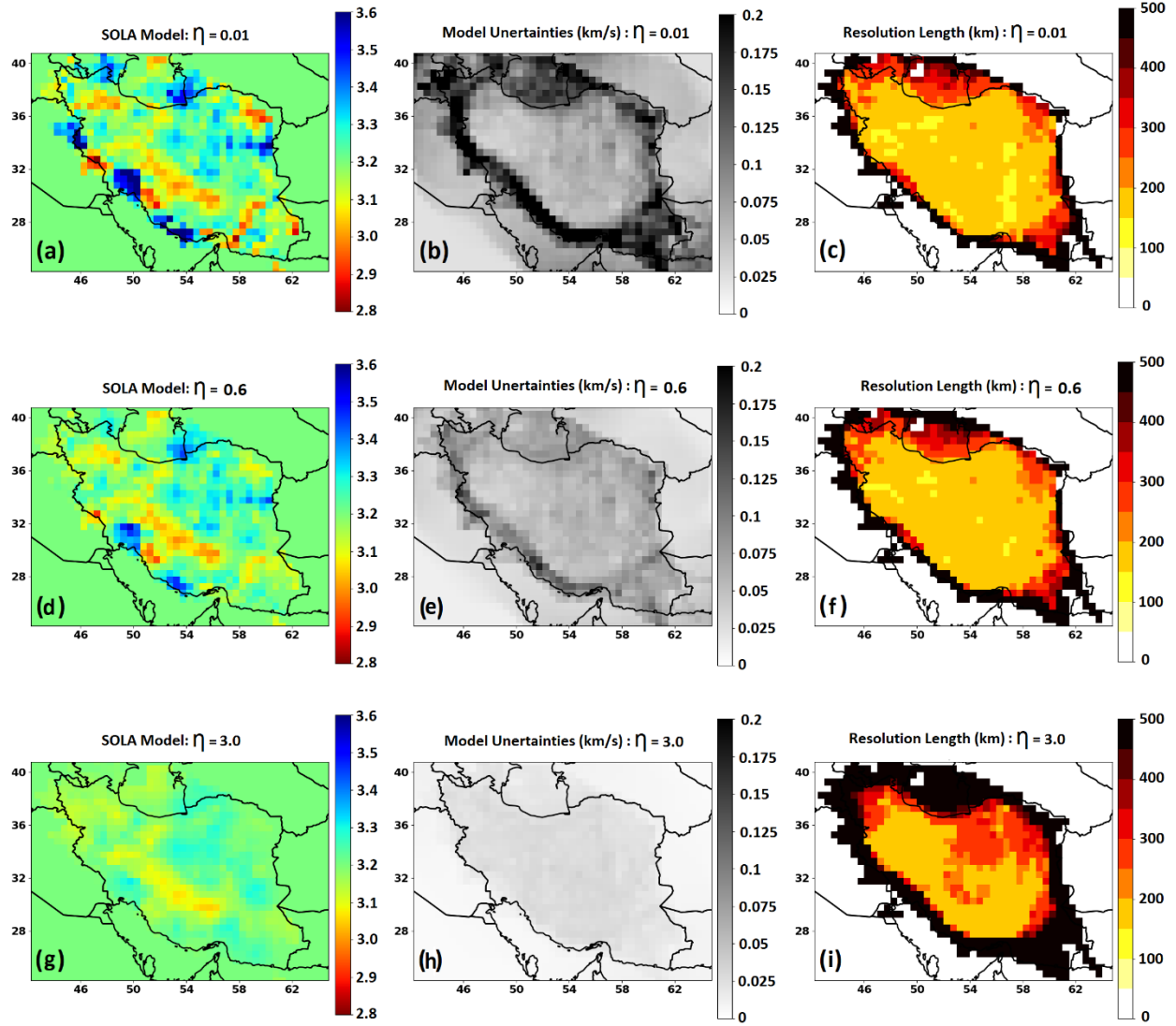
Figure 6. Tomographic model (a,d,g), uncertainty (b,e,h) and resolution length (c,f,i) maps obtained using η values 0.01, 0.6 and 3.

3-3 SOLA vs FMM

In our previous work, Amiri et al., (2023), we demonstrated that the SOLA method has many advantages when used in regions with relatively sparse and anisotropic ray-coverage, as it reduces smearing artifacts that can bias interpretation. We also found it to be advantageous in regions with good ray-coverage and weak heterogeneities, as it produces self-consistent resolution and uncertainty estimates that allow for more robust interpretations. There was one situation, however, in which SOLA did not yield optimal tomographic images: regions with strong heterogeneities and ample ray coverage. In such cases, the Fast-Marching Method (FMM) developed by Nick Rawlinson (Rawlinson, 2005) produced superior images, though lacking in the resolution and uncertainty details crucial for robust interpretation (Amiri et al., 2023). We added the FMM models into this study to enable comprehensive and precise interpretations of the Rayleigh wave group velocity models across different periods and regions. We utilized the Fast-marching surface tomography (FMST) package developed by Nick Rawlinson (Rawlinson, 2005). This method is an iterative, non-linear surface wave tomography. We determined the damping and smoothing factors of the subspace

inversion by evaluating the trade-offs between data residual and model variance, illustrated in L-curves (Supplementary Figure). For instance, in boundary regions, we prefer to interpret the SOLA model while in areas with dense ray coverage and sharp anomaly contrasts, the FMM results may take precedence.

3-4 Homogenization of resolution values

The method described above allowed us to produce 2D maps of Rayleigh wave group velocities whose resolutions are consistent with the lateral variations in path coverage and whose uncertainties are consistent with the resolutions. Each map contains the group velocities for a single period. The most logical step toward obtaining a 3D model of Vs would be to invert all the group velocities corresponding to the same location using the known sensitivities of group velocities at different periods to Vs at different depths. If we performed this inversion at this stage, however, we would be inverting group velocities with different lateral resolutions as if they had the same lateral resolution; worse, we would be inverting using group velocity uncertainty estimates that are internally inconsistent. For example, we would give a stronger weight to a group velocity in a region of poor path coverage because its larger resolution length has led to a small uncertainty (the larger the region over which we average, the smaller the uncertainty on that average), not because the group velocity estimate at that particular location is inherently more certain. To avoid this pitfall, we have added an intermediate step, which is only possible because SOLA allows us to adjust the resolution separately in each point of the model. We call this process homogenization.

To homogenize our set of group velocity maps, we consider as our benchmark the resolution values in all cells of period 50s obtained with $\eta=0.6$. We then adjust the η parameters for each of the other periods in each cell. This changes the sizes of the averaging kernels while the target kernels stay fixed for each cell (they only vary with changing ray coverage). We experimented with multiple η values for each period, and obtained the resolution value for each cell corresponding to each η. Then, we compared all computed resolution lengths for each cell with the corresponding cell's reference resolution length at 50 seconds and $\eta=0.6$ and selected the η value that reduced this difference to below 20 km. The difference maps in Fig. 7 provide insights into the quality of the final model.

For periods below 50s, we often needed to degrade the resolution to bring it closer to the reference value, this meant increasing η, which led to a decrease in group velocity uncertainty. For periods above 50s, we often needed to improve the resolution to bring it closer to the reference value; this meant decreasing η, which led to an increase in group-velocity uncertainty.

The homogenized Rayleigh wave group velocity maps are illustrated in Figure 8. As anticipated, for periods shorter than the benchmark, the final models tend to align more closely with the background model due to increased trade-off parameters and larger averaging kernel sizes in each cell. Conversely, for periods longer than 50s, the homogenized models appear more irregular due to reduced trade-off and averaging kernel sizes. We used these homogenized velocities and corresponding uncertainties as input for our shear wave velocity inversions.
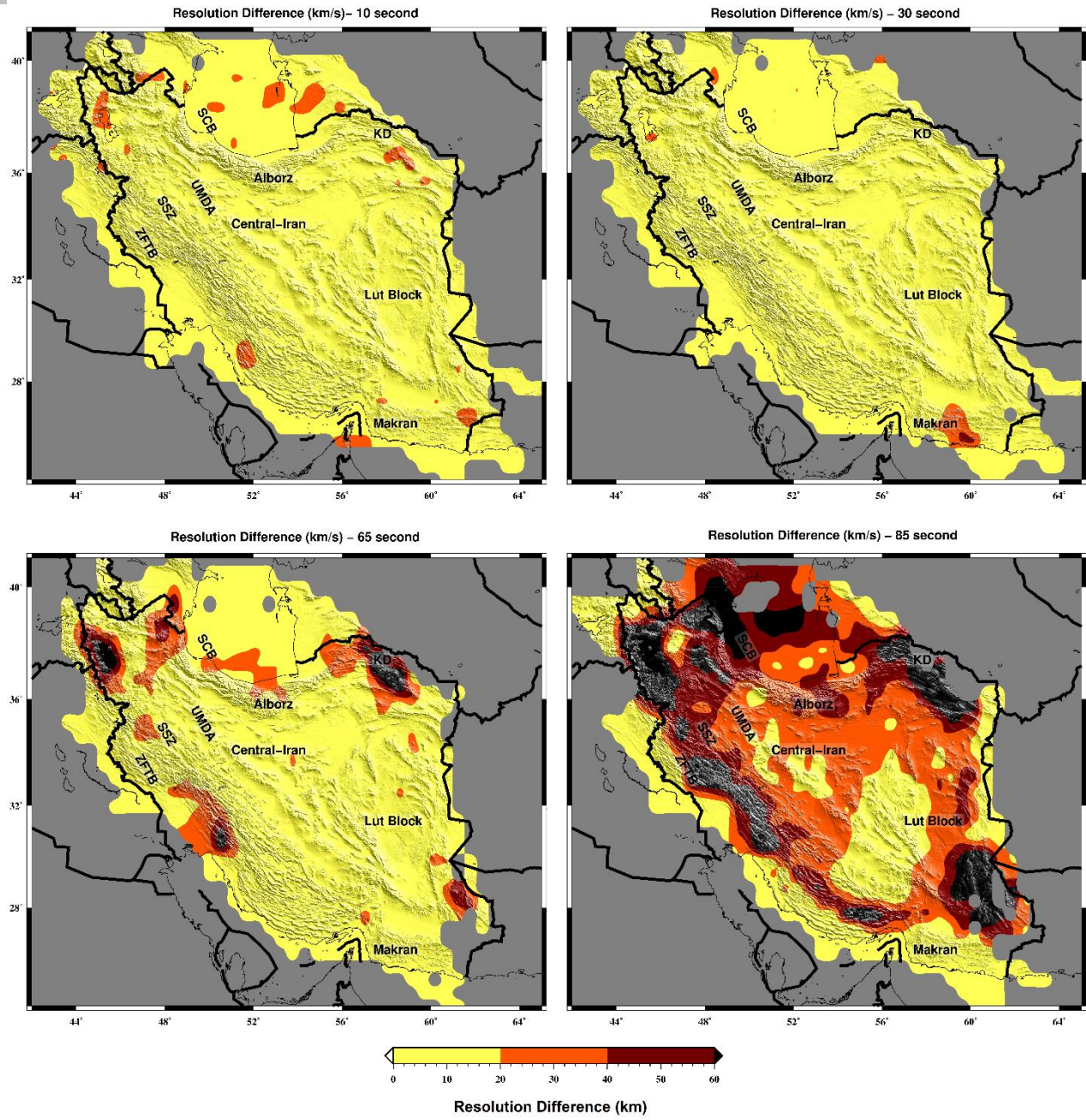
Figure 7. Maps illustrating the differences between the resolution at periods of 10, 30, 65, and 85s and the resolution at the reference period (50s). Cells with no ray paths are masked.
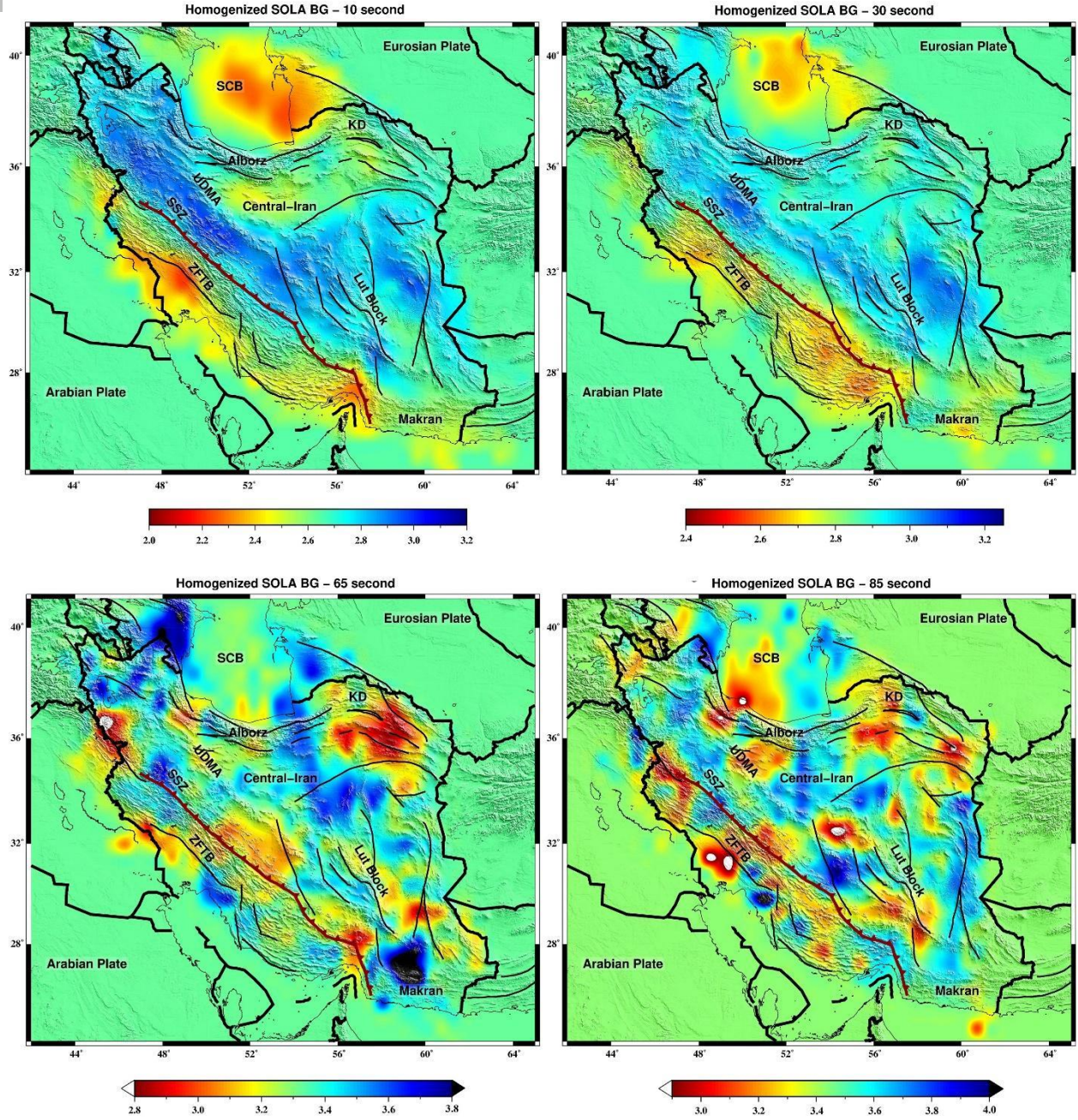
Figure 8. Homogenized group velocity maps at periods of 10, 35, 65 and 85 s.

3-5 Shear Wave Velocity Model

After extracting local Rayleigh wave dispersion curves (10–85 s) at each 0.5° × 0.5° grid cell center from the homogenized SOLA dispersion maps, we inverted them for local shear-wave velocity (Vs) models using a Bayesian Markov Chain Monte Carlo (MCMC) method (Afonso et al., 2013; Guo et al., 2016; Shen et al., 2012).

The MCMC method is well suited for nonlinear inverse problems with non-unique solutions (Sambridge & Mosegaard, 2002; Shapiro & Ritzwoller, 2002; Zigone et al., 2019; Gallagher et al., 2009; Lehujeur et al., 2018). It models the relationship between subsurface Vs structure and Rayleigh wave group velocities, then

samples a large number of candidate Vs models that fit the observations. Starting from an initial Vs model, the forward problem is solved to calculate predicted Rayleigh wave velocities, which are compared with observed values. A new model is proposed probabilistically based on the fit; better-fitting models are more likely to be accepted. Repeating this process many times produces a posterior distribution of Vs structures, from which the median model is taken as representative.

Uncertainties are estimated from the 16th (P16) and 84th (P84) percentiles of the posterior distribution, with the 68% credible interval defined as (P84 − P16)/2 (±1σ). An example Vs profile with uncertainties is shown in Fig. 9b. Compared to MCMC inversions before homogenization, we are expecting the inversions after homogenization to have lower uncertainty at shallow depths (because the resolution was forced to be poorer so the data uncertainties are smaller) and higher uncertainties at deeper depths (because the resolution was forced to be better so the data uncertainties are larger).

Initial models were parameterized from the surface to 100 km depth. Layers from 0–10 km were 2 km thick with velocities of 2.5–3.5 km/s; layers from 10–50 km were 4 km thick; and layers from 50–100 km were 5 km thick, both with velocities of 3.5–4.8 km/s. The parameterization of the 1D model used in the MCMC sampling method includes sediment thickness, 5 B-splines for crustal layering, the Moho depth, and 5 B-splines for the mantle down to a depth of 160 km. The homogenized Rayleigh wave velocities were calculated using this parameterization. P-wave velocity was obtained using a constant Vp/Vs ratio of 1.77 (Tatar et al., 2004), and density was derived from P-wave velocity using $\rho = 0.32Vp + 0.77$ (Berteussen, 1977). The sensitivity kernels of Rayleigh wave group velocities for different periods are shown in Fig. 9a. Average velocities and uncertainties at each period after homogenization are listed in Table 2.

Table 2. Average velocity and uncertainties values for different periods from SOLA inversion

Periods (s)	Average homogenized group Velocity (km/s)	Average Uncertainties (km/s)
10 Seconds	2.64	0.010
20 Seconds	2.72	0.016
30 Seconds	2.85	0.018
50 Seconds	3.19	0.032
65 Seconds	3.31	0.123
85 Seconds	3.4	0.190

Figure 9. (a) Sensitivity kernels of Rayleigh-wave group velocity at different periods. (b) Vs profile for one cell after inversion, with corresponding uncertainties.

4 TOMOGRAPHIC RESULTS

4-1 Fundamental Mode Rayleigh Wave Group Velocities

Figures 10, 11, 12, 13 and 14 depict maps of Rayleigh-wave group velocities inferred from our noise correlation and earthquake dataset, respectively for periods of 10, 30, 50, 65 and 85s using Fast-marching and SOLA tomographic methods. Accompanying them are SOLA model resolution lengths and their uncertainties for each period. In addition to mapping Rayleigh-wave group velocities using the Fast-Marching and SOLA tomographic methods, we compare our results with recent studies (Irandoust et al. 2022) that utilized better and denser ray coverage in the same region. This comparison serves as a reference

to test the thesis of Amiri et al. (2023) that Fast-Marching method produces superior images in regions with strong ray coverage and sharp anomaly contrasts and the SOLA method performs better in areas with poor ray coverage.

Periods 10 and 30s constrain the upper and middle crust (Fig. 9-a). The models in these periods show similar anomalies due to dense ray coverage but different velocities. The models show low group velocities in areas of known deep sediments: the South Caspian Basin, the Zagros Basin and most of its fold-and-thrust belt, the Makran Accretionary Wedge, and Central Iran. The low group velocities in the Zagros fold and thrust belt are related to weakening and fracturing on shallow and low-angle reverse faults because of intense deformation (Jackson and Fitch, 1981) and thick Meso-Cenozoic sediment cover. The Sanandaj-Sirjan Zone, Lut block and south of central Iran have higher velocities for the same period range. The fast group velocities of the Sanandaj-Sirjan zone are related to its metamorphic Paleozoic-Cretaceous rocks, which show little to no surface sedimentation or volcanic activity. Both 10-s velocity maps (Fig. 10a–b) show a decreasing velocity trend from the western part of the Urumieh–Dokhtar region toward Central Iran. Previous studies have attributed this relatively low velocity zone to volcanic and sedimentary rocks deposited by lava flows over pre-existing pyroclastic materials (e.g., Mottaghi et al., 2013). The Sanandaj-Sirjan Zone and the Zagros Fold and Thrust Belt are separated by the Main Zagros Reverse Fault. In the north, the Alborz region does not show particularly low velocities at shallow depths, but the western Kopet Dag has relatively low velocities in the shortest periods.

The 50 s period constrains the Moho depth and uppermost mantle. Disagreement between tomographic images is common when coverage is poor, as the priors imposed in the inversion act more strongly in the absence of data. In our damped least-squares inversion, the relatively sparse and uneven ray coverage, particularly near the model boundaries, results in a patchy appearance and generates artifacts (such as high velocity in Makran) in the FMM map at this period (Fig. 12a), with irregular block-like patterns reflecting the limited resolving power in these areas. The local resolution length is relatively low in the Sanandaj–Sirjan Zone, Urumieh–Dokhtar, Central Iran, and the Lut block, while at the edges of the model and in the South Caspian Basin the resolution length is high. Nevertheless, the South Caspian Basin is still dominated by low velocities, in agreement with previous studies. There is a discrepancy between the two maps (Fig. 12a-b) in the Sanandaj–Sirjan Zone and Urumieh–Dokhtar; as these are regions with sharp anomaly contrasts and strong ray coverage, we favor the FMM model. Our FMM model in this region is similar to that of Movaghari and Javan (2019). The Sanandaj–Sirjan Zone becomes a more prominent low-velocity region compared to lower periods. Central Iran and the Lut block show high velocity in both maps but less so in the SOLA model.

At a period of 65 seconds (Fig. 13), although there are similarities in both FMM and SOLA models, differences appear in some regions. In our SOLA model, the northwestern part of Sanandaj-Sirjan and parts of the Zagros Fold and Thrust Belt (boundary region) exhibit high velocities, while in the FMM model, the velocities in this region approach those of the background model. According to Irandoust et al. (2022), which had excellent ray coverage, the Sanandaj-Sirjan and similar parts of the Zagros Fold and Thrust Belt are high-velocity regions, supporting our SOLA model. Despite using only about a third of the number of stations as Irandoust et al. (2022), the SOLA model yields similar results in this boundary region, demonstrating the effectiveness of the SOLA technique in areas with poor ray coverage. In the Makran, both models show high velocity but in the FMM model this anomaly is smeared. The N-S shape of this anomaly in the SOLA model is completely aligned with Irandoust et al. (2022).

At the longest periods (85 seconds, Fig. 14), both FMM and SOLA models show high velocity in Central Iran and the Sanandaj-Sirjan, while the Urumieh-Dokhtar exhibits low velocity. The high velocity in the Makran zone in the FMM model is clearly an artifact and is not suitable for interpretation. Plotting SOLA

averaging and target kernels in this area effectively detects this artifact. Another artifact in the FMM model is the low velocity in the eastern part of the Lut block which in the SOLA model is resolved.
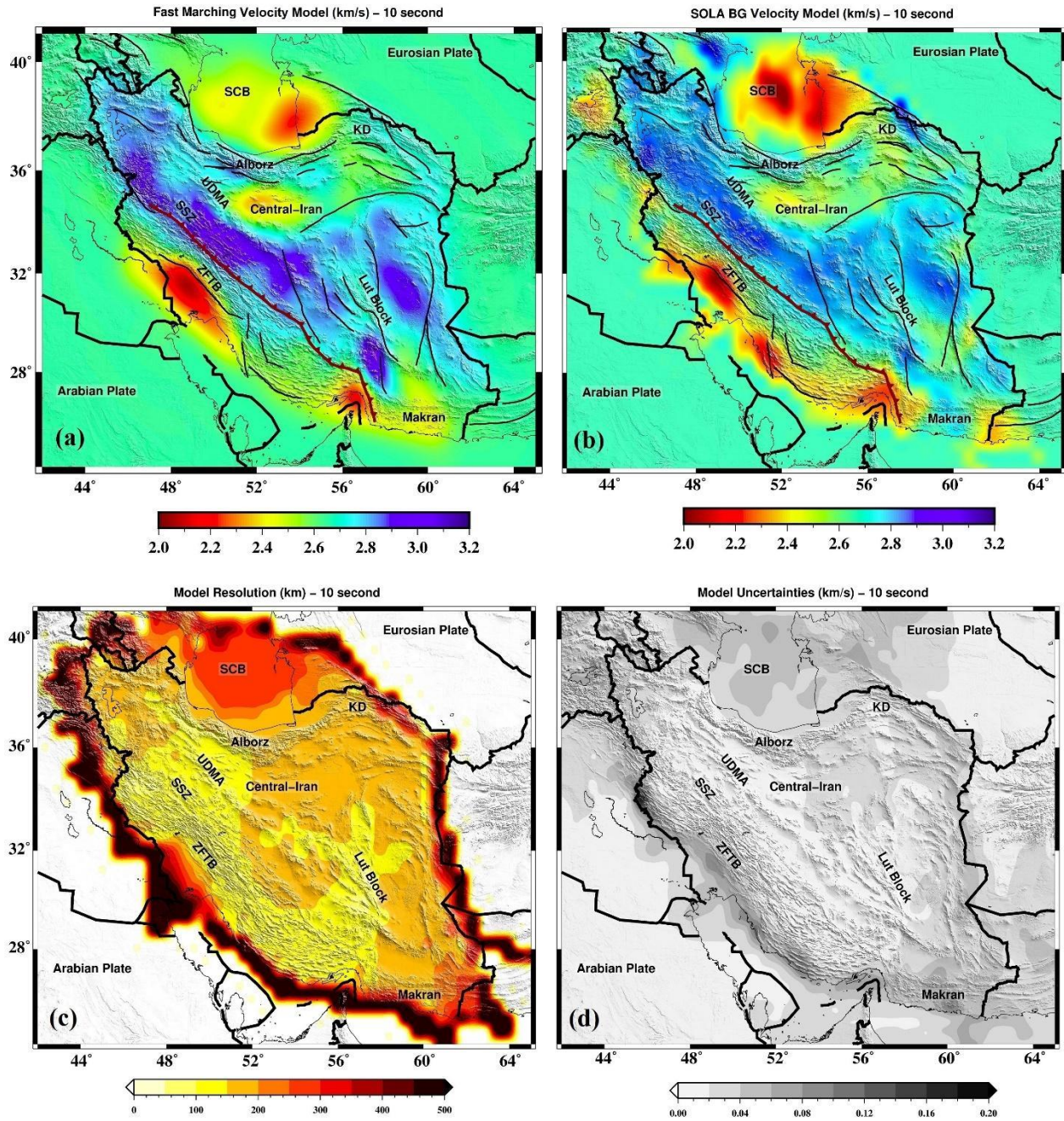

Figure 10. Tomographic results for group velocities at 10 s period. (a) Group velocity map obtained using Fast-marching tomography. (b) Group velocity map obtained using SOLA Backus-Gilbert tomography. (c) Resolution lengths and (d) model variances from the SOLA inversion.
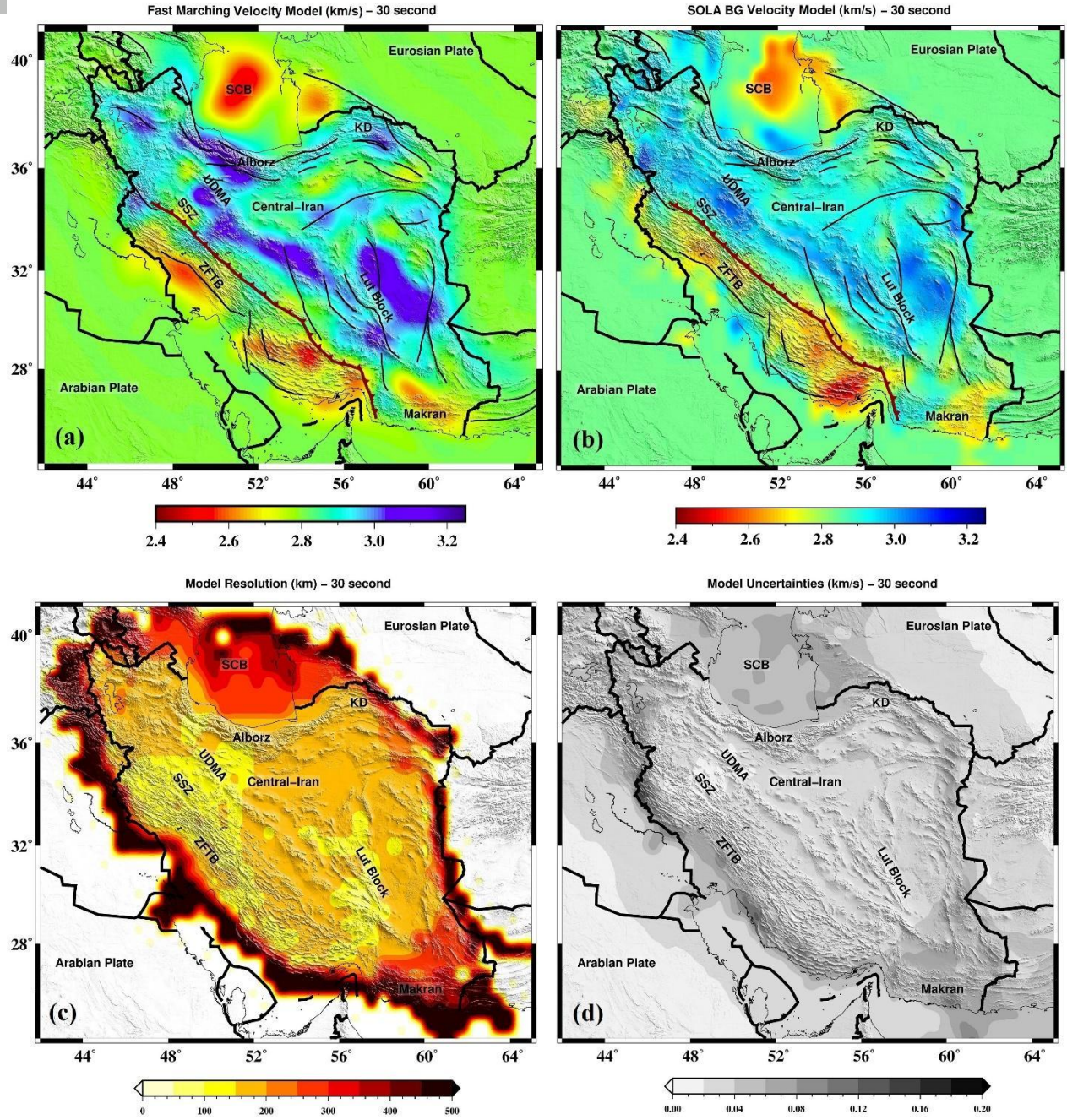
Figure 11. Tomographic results for group velocities at 30 s period. (a) Group velocity map obtained using Fast-marching tomography. (b) Group velocity map obtained using SOLA Backus-Gilbert tomography. (c) Resolution lengths and (d) model variances from the SOLA inversion.

Figure 12. Tomographic results for group velocities at 50 s period. (a) Group velocity map obtained using Fast-marching tomography. (b) Group velocity map obtained using SOLA Backus-Gilbert tomography. (c) Resolution lengths and (d) model variances from the SOLA inversion.
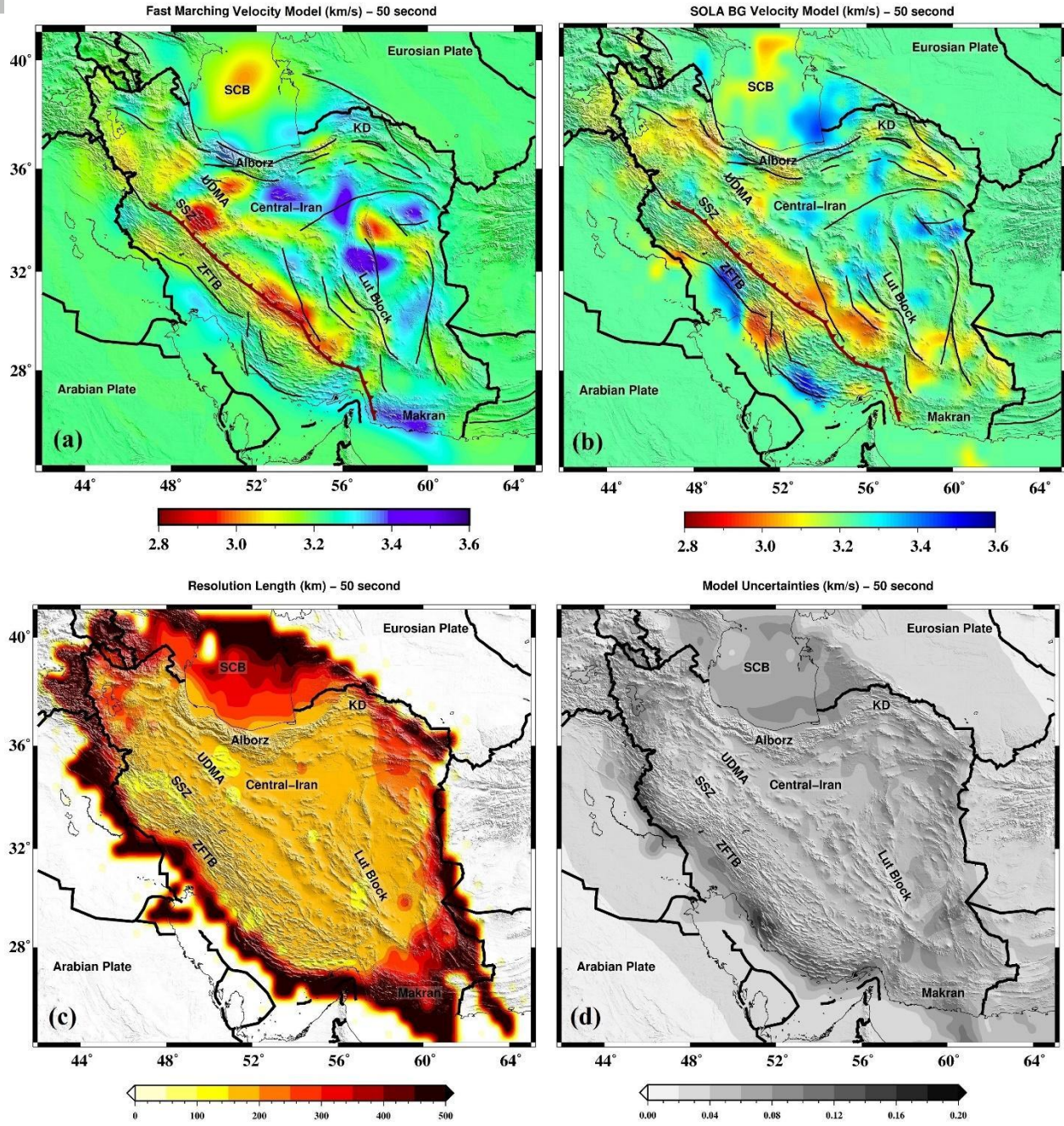
Figure 13. Tomographic results for group velocities at 65 s period. (a) Group velocity map obtained using Fast-marching tomography. (b) Group velocity map obtained using SOLA Backus-Gilbert tomography. (c) Resolution lengths and (d) model variances from the SOLA inversion.

Figure 14. Tomographic results for group velocities at 85 s period. (a) Group velocity map obtained using Fast-marching tomography. (b) Group velocity map obtained using SOLA Backus-Gilbert tomography. (c) Resolution lengths and (d) model variances from the SOLA inversion.
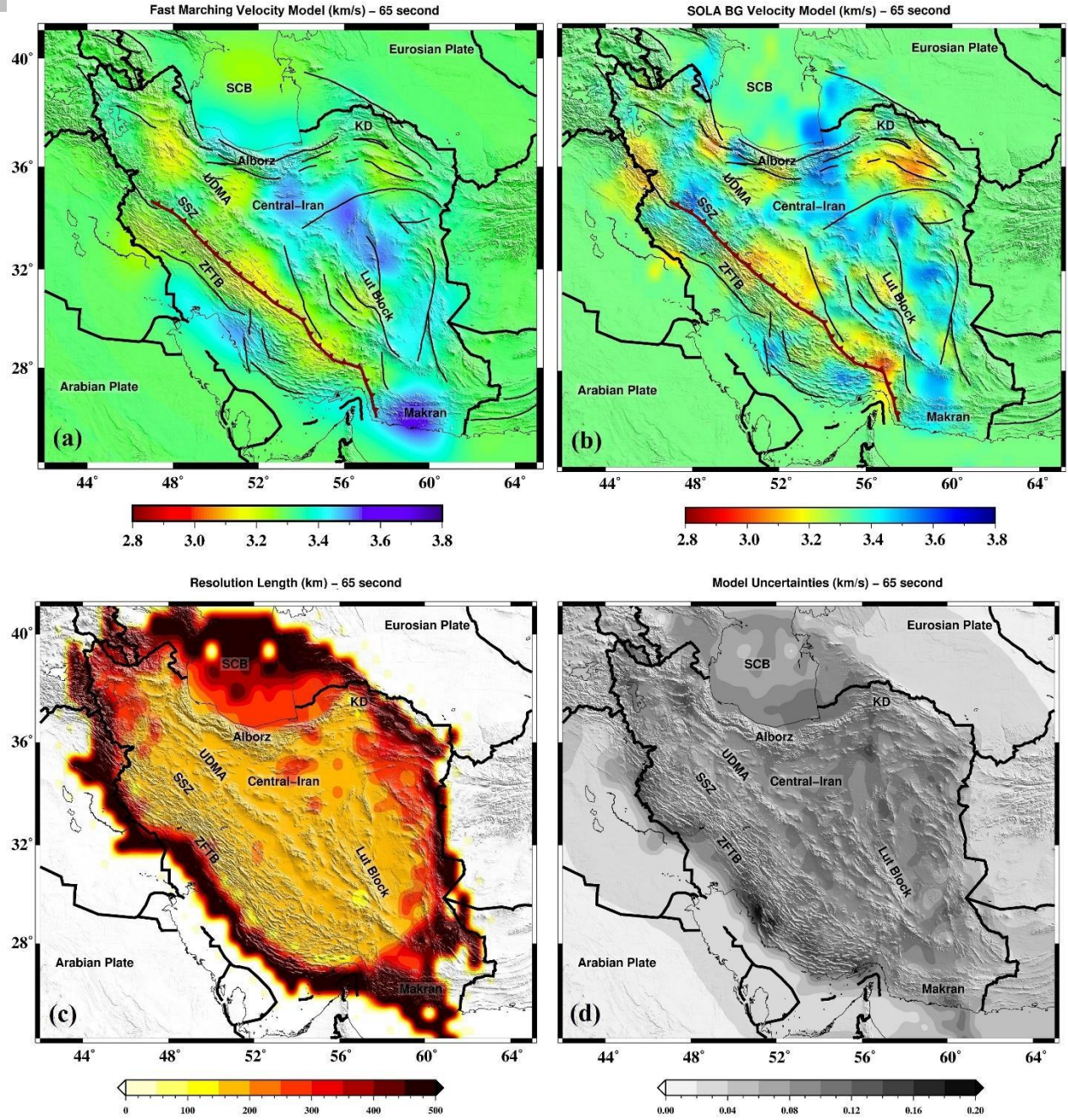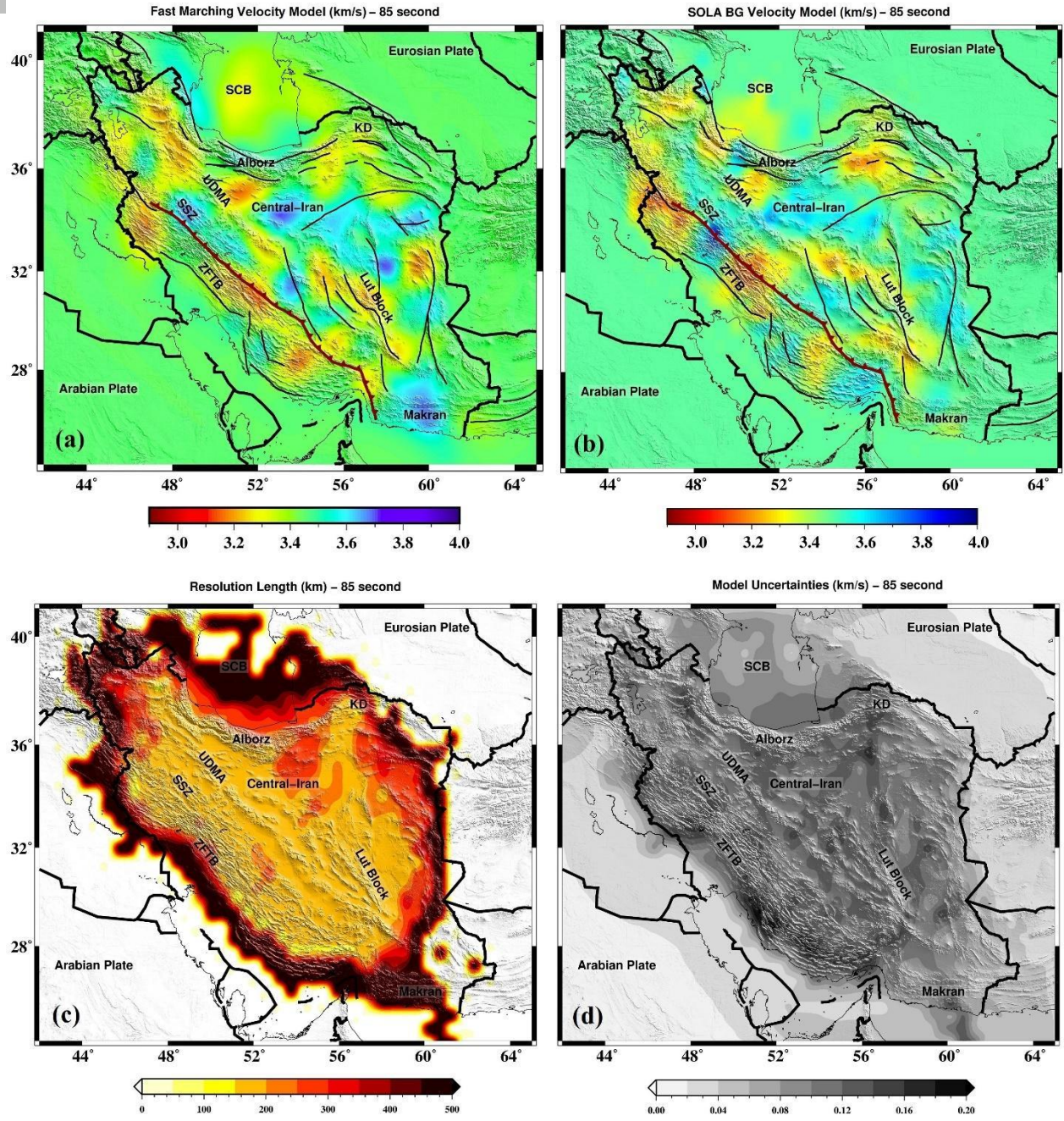
4.2 Shear Wave Velocity Maps

Fig. 15 presents shear wave velocity (Vs) and at depths of 10, 20, 40, and 60 km, representing the upper crust, middle crust, lower crust, and uppermost mantle, respectively. The Moho depth ranges from 35 to 50 km in the majority of study area (e.g., Movaghari et al., 2019; Mahmoodabadi et al. 2020; Kaviani et al. 2020; Wu et al., 2021; Irandoust et al., 2023).

At a depth of 10 km (upper crust), the lowest shear-wave velocities are associated with sedimentary basins such as the Zagros suture zone, South Caspian Basin (where these low velocities extend to around 40 km depth), and Makran. At this depth, the Main Zagros Reverse Fault appears as a boundary, separating the low-velocity region (below 3.0 km/s) of the Zagros belt from the high-velocity region (approximately 3.4 km/s) of Central Iran. Additionally, a low-velocity anomaly is observed in the eastern Alborz, extending into Central Iran.

At mid-crustal depths (20 km), central Iran, Alborz, Sanandaj-Sirjan and Urumieh-Dokhtar are characterized by high shear-wave velocities, while low velocities dominate in the Zagros, South Caspian Basin and Makran regions. The high-velocity anomaly observed in northern Makran corresponds to the shallow-dipping subduction of the Arabian Plate beneath the Oman Sea and Makran forearc. This high-velocity anomaly is most prominent at shorter periods, reflecting the thin crust (~20–30 km) in this region, and is associated with shallow seismicity (<20 km depth; Jackson & McKenzie, 1984), consistent with low-angle subduction processes (Yaminifard et al., 2007; Yaminifard & Hatzfeld, 2008). In contrast, beneath the Bazman volcanic area, east of the Jazmurian depression, we identify a low-velocity anomaly. This likely reflects a warm lithospheric wedge overlying the subducting Arabian Plate, which thickens the crust and may contribute to the magmatic sources feeding the Taftan–Bazman volcanic arc (Byrne et al., 1992).

Along the central Coastal Makran, a separate high-velocity feature is observed. Here, the high-velocity is associated with the relatively colder and denser oceanic lithosphere of the downgoing plate in the forearc, producing elevated shear-wave velocities and highlighting the structural contrast with the overlying low-velocity lithosphere of the Lut Block.

Based on geological evidence, Alavi (1992, 1994) proposes that the Atrak River valley (close to Binalud (BI) and under point B' in Fig. 1) serves as the suture zone, marking the connection between the Iranian plateau and the Eurasian plate. This area is referred to as the Neo- and Paleo-Tethyan ophiolitic suture zone (see Shafai Moghadam and Stern 2015). The low velocity around the Binalud can be attributed to this suture zone. Our findings in northeast Iran align well with the Motaghi's et al. (2012b) results in this region.

At a depth of 40 km, the contrast between the high-Vs, low-topography region of central Iran and the surrounding low-Vs mountainous regions become more pronounced. The Makran Subduction Front emerges as a high-Vs area, while its volcanic arc region exhibits low Vs. The South Caspian Basin remains a low-Vs region extending into mantle depths. In the central and southern Zagros, a low-velocity zone extends toward central Iran, whereas in the northern Zagros, it is confined to the Main Zagros Reverse Fault. This may indicate different underthrusting patterns of the Arabian plate beneath the Iranian plate in the central, southern, and northern Zagros. Previous studies (e.g., Al-Lazki et al., 2004; Maheri-Peyrov et al., 2016) have already reported these varying underthrusting patterns along the Main Zagros Reverse Fault.

At a depth of 60 km, most of the map is characterized by high velocities. In particular, Vs values are generally elevated in both the Zagros Fold and Thrust Belt and the Makran subduction zone. Across all depths shown in Fig. 15, the Jazmurian Depression and the Lut Block to the north consistently appear as relatively high-velocity zones. The most pronounced low-Vs anomaly in the upper mantle occurs beneath the southwestern margin of the South Caspian Basin, along with another low-velocity feature in the central

Sanandaj-Sirjan zone. Motaghi et al. (2018) identified reduced shear-wave velocities beneath the Alborz–Talesh transition zone and interpreted them as reflecting the lithospheric boundary between the southwestern South Caspian Basin and the southern Talesh Mountains. Similarly, Rastgoo et al. (2018) imaged a low-Vs anomaly beneath the western Alborz at depths of 50–100 km, attributing it to post-collisional delamination of the lower lithosphere. Our results align with these observations but indicate that the anomaly extends across a broader region, encompassing both the southwestern South Caspian Basin and the western Alborz. The low velocities in the Sanandaj-Sirjan zone are likely linked to elevated lithospheric temperatures and potential partial melting associated with subduction-related processes and magmatism, consistent with earlier seismic and tectonic studies (e.g., Maggi & Priestley, 2005; Motaghi et al., 2015; Irandoust et al., 2022).
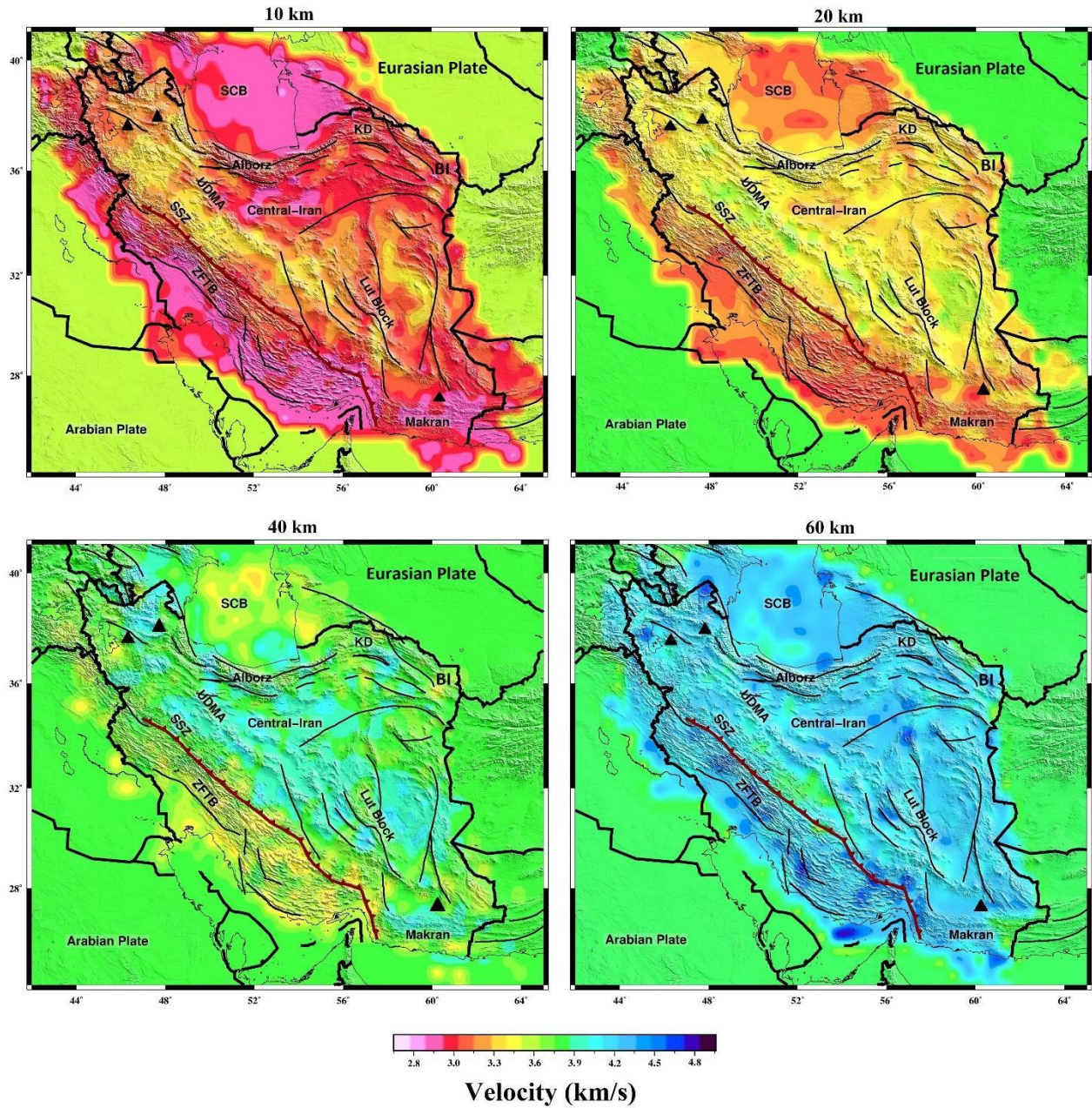

Figure 15. Variations of shear-wave velocity at representative depths.

5 DISCUSSION

5. 1 Depth Variations of Vs, uncertainties and resolution length in the Crust and Uppermost Mantle

We inverted Rayleigh wave group velocities to generate an updated model of the crust and uppermost mantle Vs structure of the Iranian Plateau. Our high-resolution maps exhibit significant anomalies which mainly are consistent with previous studies (e.g., Talebi et al., 2025; Yang et al., 2023; Irandoust et al., 2022; Kaviani et al., 2020; Mohammadi et al., 2013a and b; Mortezanejad et al., 2018; Motaghi et al., 2015; Shad Manaman & Shomali, 2010; Shad Manaman et al., 2011). For each location, we ensure consistent lateral resolution at different periods, an approach used here for the first time, and invert for shear wave velocity as a function of both depth. We have created four cross-sections perpendicular to key regions to visualize subsurface variations in Vs and their uncertainties, explore lateral and vertical heterogeneities, and relate them to geological or tectonic structures (see Fig. 1 to for location of the cross-sections). We choose cross-sections that intersect perpendicularly with active seismotectonics units and significant faults. Profiles AA' and BB' (Fig. 16 and 17) cross regions of good ray coverage and enable comparisons with previous studies; profiles CC' and DD' (Fig. 18 and 19) cross poorly-studied regions like the Koph-Dagh, Sistan suture zone, and Jazmurian depression.

In all profiles, we present the Vs structure down to 100 km depth, accompanied by its corresponding uncertainty map and resolution lengths. The uncertainties in all sections are mostly below 0.2 km/s, indicating a reliable level of confidence for Vs interpretation. We also display lateral resolution lengths at selected representative locations near key anomalies, to provide additional context on the spatial resolving power at those points. In this study, we use a shear wave velocity of 3.3 km/s as the upper limit for sediments. This threshold is consistent with previous seismic studies in the region (e.g., Motaghi et al., 2018; Movaghari et al., 2019., Irandoust et al., 2022). The Vs of the uppermost mantle beneath the Plateau is mostly in the range of 4–4.3 km/s which is similar to other comparable deforming regions such as the Anatolian Plateau (e.g., Kaviani et al., 2020; Koulakov, 2011; Maggi & Priestley, 2005; Salaün et al., 2012).

5.2 Profiles AA' and BB'

In profile AA', the resolution length values are relatively consistent and low due to the strong and uniform ray coverage along profile but is maximum at the end of the profile (109 km) because, ray coverage dropped slightly near the boundary of the model in Alborz whereas along profile BB', the resolution increases from the Zagros to the end of the profile (Binalud). This variation is also due to the sparser ray coverage toward the northeastern part of Iran (the end of profile BB').

5.2.1 Shallow Crust

The Zagros, Sanandaj-Sirjan Zone and Urumieh-Dokhtar

The upper crust in both AA' and BB' profiles (Fig. 16 and 17) show the lowest velocity values of all the profiles. The Zagros have a very thick sedimentary cover in the upper crust that might be attributed to the Cambrian and Miocene sediments, with more than 10 km thickness in some regions (Stocklin 1974; Stoneley 1990; Talebian & Jackson 2002; Hatzfeld et al. 2003). Low velocities in Zagros upper crust could also be related to the active crustal deformation as inferred by Yang et al., (2023a and b) who found low crustal Q_{Lg} beneath the Zagros orogen. This is further supported by Kreemer et al. (2014), whose global strain rate model highlights elevated strain rates localized in the northern and southern Iranian Plateau, including the Zagros orogen, and the decreasing GPS velocity from the Zagros orogen toward the northern Iranian Plateau (e.g., Khorrami et al., 2019). The high-velocity anomaly in profile BB′ beneath parts of the

Sanandaj–Sirjan Zone and Urumieh–Dokhtar (A1) aligns with observations of a low attenuation coefficient (Irandoust et al., 2016; Ahmadzadeh et al., 2017; Fard et al., 2019; Movaghari et al., 2019) and relatively low seismicity compared to the Zagros zone. This contrast arises because the Zagros comprises deformable sediments and active thrusting, whereas the Sanandaj–Sirjan and Urumieh–Dokhtar regions are mainly metamorphic terrains with extensive Mesozoic magmatism and abundant volcanic and intrusive rocks (Movaghari et al., 2019), which contribute to the observed high-velocity anomaly. Irandoust et al. (2016) reported a difference of 42 in Q_0 between the two regions indicating that these contrasts reflect the Zagros being a more attenuating medium than the Sanandaj–Sirjan and Urumieh–Dokhtar.

The age distribution of igneous rocks divides the Urumieh-Dokhtar into northwestern, central, and southeastern parts. Magmatism in the central Urumieh-Dokhtar is older than the volcanic activity in the NW and SE (Chiu et al., 2013). The age of the volcanism correlates well with Lg attenuation, with low QLg observed in the older central Urumieh-Dokhtar compared to the younger regions on either side (Chiu et al., 2013). The A1 beneath UDMA in profile B aligns with the central Urumieh-Dokhtar, which represents an older block with low attenuation, in contrast to the UDMA in profile A (northwestern Urumieh-Dokhtar), a younger and more attenuative region. With age, magmatic bodies cool, crystallize, and become mechanically stronger, resulting in reduced attenuation and higher Vs velocities in the central Urumieh-Dokhtar.

In both profiles, higher Vs uncertainties are visible at the depth of 10 km due to velocity jump from lower to middle crust. This trend started from Zagros to central Iran.

Central Iran

Central Iran shows a thicker zone of low-velocity upper-crust (10 km) on profile AA' than on profile BB'. Our results show thick, shallow sedimentary deposits in Central Iran characterized by shear wave velocities below 3.3 km/s, which has been confirmed by many studies: Movaghari et al. (2021), Irandoust et al. (2022), Kaviani et al, (2020). Toward the North-East, near the Alborz (A2), this low-velocity zone narrows and is juxtaposed with a distinct high-velocity anomaly in the upper crust, which will be further discussed in the Alborz section.

Teknik and Ghods (2017) estimated variable depths of the magnetic basement across Central Iran from about 7 km in the Great Kavir sedimentary basin, located in the north of Central Iran, to about 13 km near the Alborz margin, likely due to the thick sedimentary layers (near AA' profile). Other studies found sedimentary thicknesses not exceeding 10 km in much of Central Iran (e.g., Morley et al., 2009; Mousavi & Ebbing, 2018; Soffel & Förster, 1984). Our finding of ~10 km thickness in AA' is in good agreement with these studies and is similar to the profiles of Kaviani et al. (2020) and Movaghari et al. (2019), which also indicate a low-velocity zone (<3.3 km/s) of around 10 km thickness beneath Central Iran.

In a recent study, Zarunizadeh et al. (2025) constructed a 3-D S-wave velocity (Vs) model for Iranian plateau by inverting phase velocity dispersion data from teleseismic Rayleigh waveforms. The results from their E profile confirm our results in BB'.

Alborz and Binalud

The shear-wave velocities everywhere in the shallow crust (<10 km) throughout the width of the Alborz are slightly higher than in neighboring regions. A part of Alborz (A2) shows higher Vs in the shallow crust along the AA' profile (Figure 16). This observation aligns with the findings of Yang et al. (2023a, b), who reported normal to low seismic attenuation in the Alborz region. These low attenuation zones, often associated with more consolidated and crystalline crustal materials, are mainly located around igneous

outcrops. Movaghari et al. 2019 also attributed this high velocity zone to the presence of volcanic and intrusive rocks.

The uppermost crustal low-Vs anomaly (below 3.3 km/s) beneath the Binalud and north-eastern edge of Central Iran and north of Lut block limited to ~10 km depths, in agreement with the sedimentary layer obtained by magnetic study by Mousavi and Ebbing (2018). Also, Irandoust et al. (2022) reported 7 to 10 km upper crust depth the shear wave velocity between 3 to 3.4 km/s, similar to result reported by Kaviani et al. (2022). Yang et al. (2023b) obtained very low quality-factor (< 200) beneath of this area which confirmed our findings. This low Q_{Lg} is related to storage-transport processes of the ascending melt. In the Lut Block, diffuse magmatism is almost continuous from the Early Cretaceous to the Quaternary (Jentzer et al., 2020). The formation of Lut volcanism may be related to WE-dipping Sistan Oceanic subduction (e.g., Moghaddam et al., 2021; Saccani et al., 2010) and lithospheric delamination during the Lut-Afghan collision (Pang et al., 2013).

Motaghi et al. (2015) reported the upper crust beneath Binalud has an S-wave velocity between 2.5-3.4 km/s. The thick (~10 km) sedimentary basins (Afshar-Harb, 1979; Lyberis & Manby, 1999; Robert et al., 2014; Teknik & Ghods, 2017), and the dense seismically-active faulting system of NE Iran (e.g., Aflaki et al., 2019; Hollingsworth, Fattahi, et al., 2010; Shabanian et al., 2012) explain the low-Vs upper crust in this region. Irandoust et al. 2022 and Kaviani et al. 2020 reported finding similar to ours.

5.2.2 Crustal Thickening (Moho depth)

Following the onset of the Arabia–Eurasia continental collision approximately 22 million years ago during the Early Miocene (Molinaro et al., 2004), the continued convergence of plates resulted in the shortening and thickening of the Arabian crust. This process contributed to the formation of the observed high topography in the Zagros belt. The impact of this thickening is evident in the shear wave velocity sections beneath the Zagros.

Regions exhibiting low shear wave velocity (less than 4.1 km/s in both transects as a crust-upper mantle interface velocity) indicate a thick crust beneath the Sanandaj-Sirjan. This influence extends to crustal depths of approximately 55 km along profile AA' (M) and ~72 km along the profile BB' (L1). These crustal thickenings (L1) and (M) in transects may be attributed to crustal doubling beneath the Sanandaj-Sirjan (Paul et al., 2010) due to under-thrusting of Arabian Plate beneath the Central Iran. The depth of this anomaly in profile BB' surpasses previously reported crustal thicknesses in studies by Shad Manaman et al. (2011), Motaghi et al. (2017a, b) and Kaviani et al. (2020) while it is aligned with Movaghari and Javan (2019). The crust northeast of the Sanandaj-Sirjan is relatively thin (~45 km) beneath the Urumieh-Dokhtar. This indication may suggest that the Arabian lithosphere has not affected the crust beneath the Urumieh-Dokhtar. In the rest of transect AA', crustal thickness is relatively constant at ~40 km; it increases beneath the Alborz up to ~50 km.

Along profile AA′, the Moho depth in the southwest and northeast of the Alborz, where uncertainties are higher, appears greater than in the central part of the Alborz. The lateral distance from the southwest to the central part is ~100 km. In the Alborz, where uncertainties are lower (<0.2 km/s), the Moho depth is estimated at ~45 km. The lateral resolution of our inversion in this region is ~109 km. Although features smaller than this length are smoothed, the distance from the southwest to the central part (~100 km) is comparable to the resolution length, and the low uncertainty indicates that the ~45 km estimate reliably represents the average Moho depth across the Alborz. In contrast, the deeper apparent Moho toward the southwest and northeast should be interpreted with caution due to higher uncertainty and lower resolution. Previous studies using receiver functions and joint inversions reported somewhat larger crustal thicknesses (e.g., Sodoudi et al., 2009: 51–54 km; Radjaee et al., 2010: 55–58 km; Abbassi et al., 2010: ~58 km), while

more recent studies (Irandoust et al., 2022; Movaghari et al., 2021) and the and Kaviani et al. (2020) are consistent with our results. The differences between our results and some previous studies likely reflect differences in data coverage, methods, and lateral averaging in the inversions. Although, for southern and central parts of Alborz these differences are small.

We obtained similar results for the profile BB', where the crustal thickness varies from 40 to 50 km. The Moho depth in central Iran is relatively flat around ~45 km, but beneath its northeastern edge it increases to ~50 km. West of the Binalud, moho depth reaches approximately 48 km depth. In Irandoust et al. (2022), the Moho depth in central Iran and the Lut Block does not exceed 50 km, whereas it deepens to ~58 km north of the Doruneh Fault and then decreases to around 50–52 km under the Binalud. Movaghari and Javan (2019), with profile similar to BB', estimated increasing moho depth trend from center of central Iran to Binalud. The depth beneath center of the central Iran to Doruneh Fault varied from ~35 km to around 50 km and then became constant to around 50 km beneath Binalud. Also, similar results were obtained by Kaviani et al. (2020) who found a Moho depth of ~45 km beneath east of the Doruneh Fault and the Binalud.

Interestingly, the variation in Moho depth does not correlate with changes in topography; instead, the deepest Moho boundary (crustal root) is situated beneath the Sanandaj-Sirjan. The shear wave velocity variation with depth along the BB' profile aligns with findings from prior studies on crustal thickness (Irandoust et al., 2022; Kaviani et al., 2020; Movaghari and Javan, 2019, Motaghi et al., 2015, Shad Manaman et al., 2011). Previous research indicates that the crustal thickness peaks at approximately 65 km beneath the Sanandaj-Sirjan and the Urumieh-Dokhtar, then decreases to ~35 km beneath the central Iran along the profile (Motaghi et al. 2015). The thinnest Moho boundary for the central Iran was proposed by Motaghi et al., (2012a), at ~27 km depth, using migrated P-to-S converted waves.

5.2.3 Uppermost Mantle

According to previous studies on the Arabia-Eurasia collisional zone, it has been proposed that approximately 10-12 million years ago, subsequent to the onset of the collision, the lower segment of the lithosphere of the Arabian Plate underwent detachment and descended into the mantle (Molinaro et. al, 2004). This detachment process facilitated the upward migration of low-density asthenospheric materials from the mantle towards the upper layers, thereby replacing materials within the subcrustal lithosphere (Molinaro et al., 2004; Hafkenscheid et al., 2006; Hatzfeld and Molnar, 2010; ShadManaman and Shomali, 2010; Mahmoodabadi et al. 2020; Veisi et al. 2021; Kaviani et al., 2021, Yang et al. 2023b).

We have identified a region of low velocity (B1) in profile AA', situated north of the Zagros Fold and Thrust Belt, just southwest of the Sanandaj-Sirjan. This zone potentially signifies the presence of upwelled asthenosphere, coinciding with the highest elevations observed in the Zagros Mountains. The decrease in velocity may also indicate an accumulation of weaker crustal material within the orogenic wedge. Similar findings have been observed at comparable depths by Shomali et al. (2011) and Mahmoodabadi et al. (2020), suggesting an upwelling of asthenosphere into the sub-crustal lithosphere. Aftabi and Atapour (2000) report samples of potassic and ultrapotassic volcanism, which could be related to asthenospheric upwelling (e.g., Chen et al., 2017) and delamination (Kay and Kay, 1993). The presence of such a weak zone (B1) between the Zagros and the Sanandaj-Sirjan lithospheres causes less deformation of the overriding plate during convergence. The substantial topography (around 3 km) above the low-velocity anomaly B1 could imply that this elevation is supported by the upwelling asthenosphere. Additionally, a significant negative Bouguer gravity anomaly of −200 mGal is noted in this area (e.g., Mousavi and Ebbing, 2018), although the crust is not at its thickest value in this collision zone. A consistent Moho depth of ~ 45 km may imply that the upwelling of hot asthenosphere has played a significant role in forming such high topography in northern

part of Zagros Fold and Thrust Belt relative to un-thickened crust of this region. Furthermore, our uncertainties map in this area shows low velocity uncertainties.

In the AA' cross-section, a notable high-velocity zone with low uncertainty is observed in the upper mantle beneath the Zagros (H1), likely representing the Arabian lithosphere, extending to depths exceeding 100 km. These findings align with the upper mantle velocity model of the Middle East derived from surface wave analysis by Priestley et al. (2012), as well as the shear wave velocity models reported by Movaghari et al. (2021) and Mahmoodabadi et al. (2020), which utilized seismic ambient noise and joint inversion of surface wave dispersion and teleseismic P-wave Coda. The H1 anomaly appears distinct from the low-velocity anomaly beneath the SSZ (B1). H1 dips northwards below B1 and reaches its deepest point beneath the Sanandaj-Sirjan. The higher S-wave velocity observed in the uppermost mantle beneath the Zagros (H1) and SSZ, particularly beyond 60 km depth, indicates the presence of a potentially colder and stronger lithospheric mantle compared to Central Iran. This finding is corroborated by the works of Movaghari et al. (2021), Mahmoodabadi et al. (2020), Motaghi et al. (2015) and Yang et al. (2023b).

The presence of a low shear wave velocity anomaly, labeled as B2 in profile AA' and L2 in profile BB', beneath the southwest region of Central Iran, may be attributed to the upwelling of hot asthenosphere (Priestley and McKenzie, 2006; Al-Lazki et al., 2004; Maggi and Priestley, 2005; Mahmoodabadi et al., 2020) or the presence of partially molten materials (Paul et al., 2010). This hypothesis finds support in the evidence of upper Miocene to Plio-Quaternary volcanic activities observed along the UDMA, occurring subsequent to the initiation of the collision (Omrani et al., 2008; Chiu et al., 2013). The presence of a low-velocity anomaly south of the UDMA and west of the Central Iran (B2) further supports the hypothesis of upwelling asthenospheric materials.

In profile BB', low velocity anomaly L2 and the low velocity in the upper crust of northeastern central Iran suggest upwellings from the uppermost mantle to the crust, which is consistent with previous velocity and attenuation tomographic images (e.g., Amini et al., 2012; Hearn, 2022; Kaviani et al., 2022; Pei et al., 2011; Yang et al., 2023b). L2 may be related to southeast UDMA young magmatism (Yang et al. (2023a and b)). The lower velocity zones near the southeastern UDMA (L2 and B2) were also revealed in previous Pn and Sn velocity tomography (e.g., Al-Lazki et al., 2004; Pei et al., 2011). Resolution values for (B2 and L2) are 91 and 110 km, respectively due to the stronger ray coverage in AA'. Regarding uncertainties in uppermost mantle, the portion of higher uncertainties become higher in comparison shallow depth which is related to homogenization process.

Seismic evidence in other studies, including high-quality factor (Irandoust et al., 2016) and high Pn velocities (Al-Lazki et al., 2003, 2014; Yang et al., 2023 a and b) beneath the Zagros and the SSZ, along with high Sn-attenuation (Gök et al., 2003; Al-Damegh et al., 2004) and low Pn velocities (Al-Lazki et al., 2003, 2014; Yang et al., 2023 a and b) beneath the UDMA and Central Iran, collectively indicate a colder and potentially stronger lithosphere beneath the Zagros, in contrast to the weaker lithosphere found beneath the UDMA and Central Iran. Furthermore, petrological evidences support the presence of a weak uppermost mantle beneath the UDMA and western Central Iran. High-silica adakitic magmatism since the Late Miocene is interpreted as melts due to slab breakoff in the central part (Omrani et al., 2008). However, a different type of adakite with low-SiO2/high-MgO is reported in the NW (near the location of our profile) and SE UDMA (Omrani et al., 2008). It is suggested that felsic melts from the slab modifies the composition of peridotitic melts from the mantle wedge and results in this type of adakite (Stern and Kilian, 1996; Martin et al., 2005).
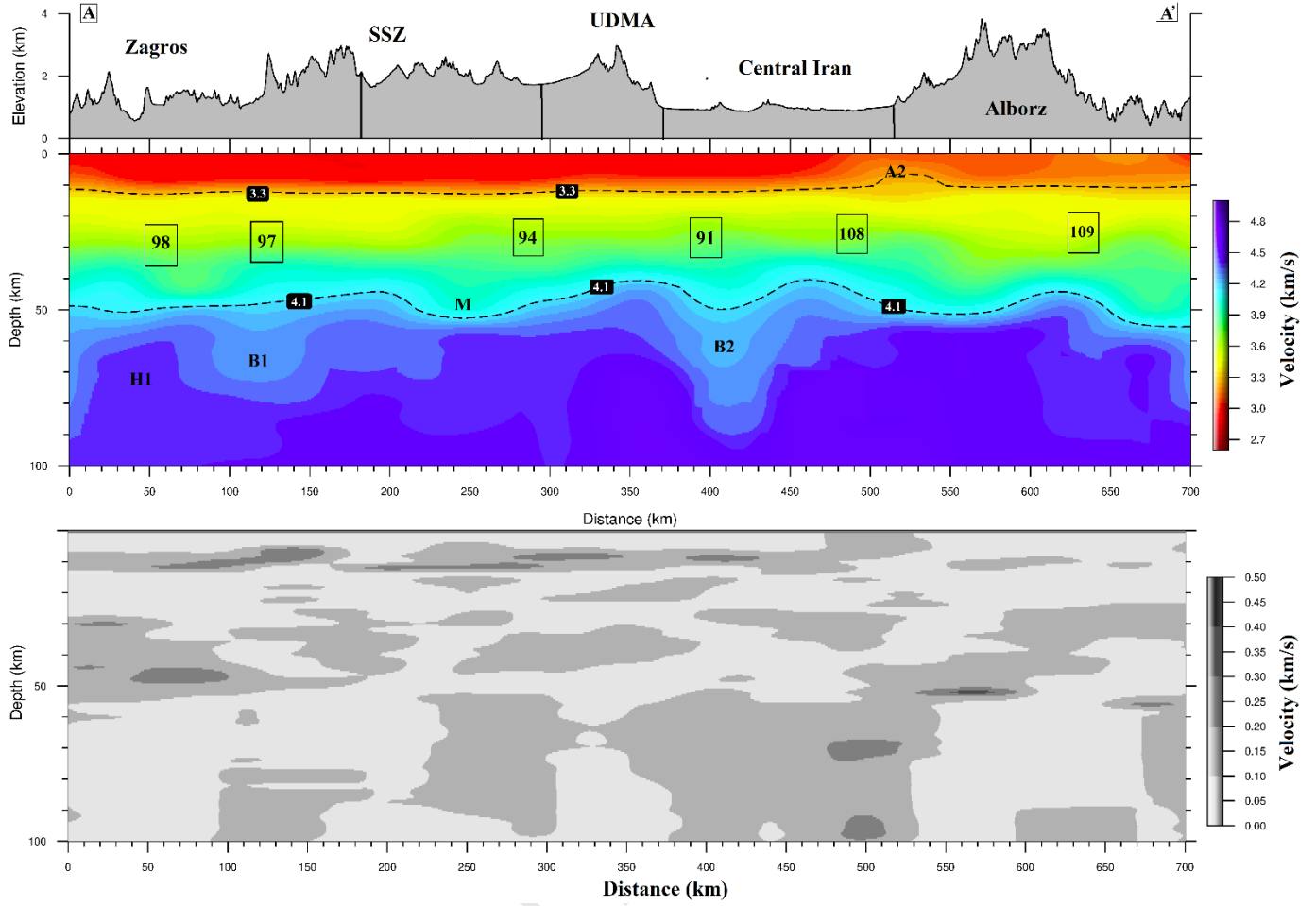
Figure 16. Transect along profile AA′ show shear wave velocities (top) and their associated uncertainties (bottom). The values in rectangles show local resolution length in that point. The locations of the profiles are given in Figure 1.
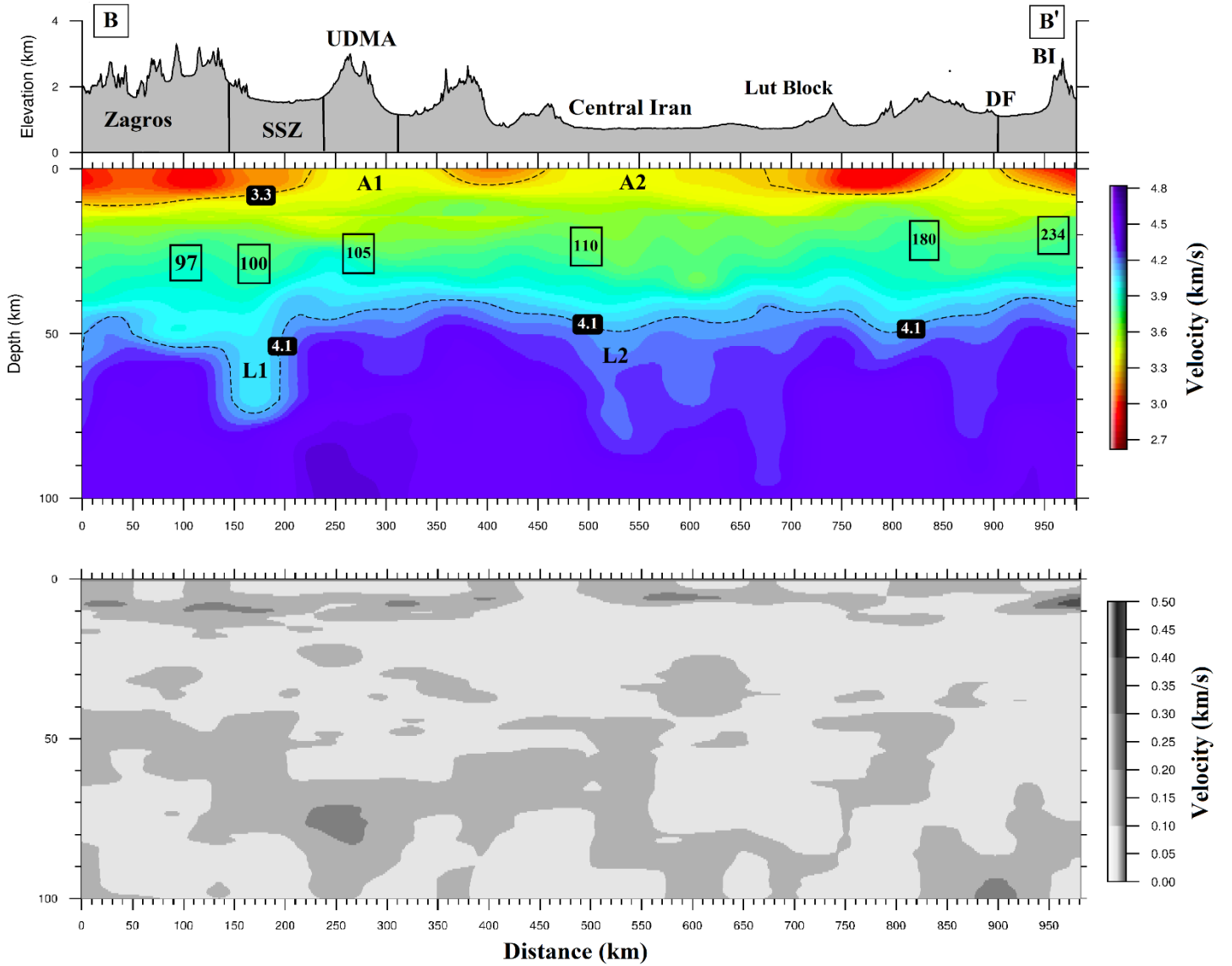
Figure 17. Transect along profile BB′ show shear wave velocities (top) and their associated uncertainties (bottom). The locations of the profiles are given in Figure 1.

5.3 Profile CC'

In this profile, which extends from the southeastern to the northeastern border, both Vs model uncertainties and resolution values are presented. The lateral resolution appears to be primarily influenced by the density of ray coverage. Starting from the Oman Sea (the southeastern boundary of our model) the resolution length is high, then decreases over the Lut Block where ray coverage improves, and increases again toward the northeastern edge of the model. As shown in Figures 1, 17, and 18, the endpoints of profiles BB' and CC' meet each other near the Doruneh Fault (labeled DF in the figures). This suggests a correlation between lateral resolution length and uncertainty values beneath of this point.

Along the entire profile, uncertainty values rarely exceed 0.2 km/s, similar to the two previously discussed profiles. The relatively high uncertainties observed in the upper crust (depths <10 km) are likely due to velocity jumps at those depths. In deeper structures, two zones of elevated uncertainty align with low-

velocity regions, possibly indicating that the homogenization process and the reduction in averaging kernel size may have negatively impacted the reliability of these values.

5.3.1 Crust and to Moho

Coastal Region and Western Makran

Profile CC' cuts across key geological features, including the Makran Subduction Zone, the Jazmurian Depression, and the Lut region. The Makran Subduction Zone (MSZ), which extends from southeast Iran to southern Pakistan, includes an accretionary wedge where the Tethys oceanic lithosphere connected to the Arabian Plate is subducting beneath the Eurasian Plate (e.g. Farhoudi & Karig 1977; Sengor et al. 1988; Byrne et al. 1992). In this profile, we concentrate on the western segments of the Makran subduction zone, located on the Iranian plateau, known for its unusually low levels of seismicity. Beneath this profile, a thick low-velocity zone (Vs < 3.3 km/s) is observed, starting from a depth of approximately 22 km below the Oman seafloor and extending to about 27 km beneath the onshore Makran area. However, this low-velocity layer thins to around 17 km beneath the southern edge of the Jazmurian Depression. This observed thick low velocity zone, particularly near the western termination of the subduction zone, reflects the large-scale geometry of the accretionary wedge. A recent receiver function/surface wave analysis by Priestley et al. (2022) along a south-north transect in the region of Chabahar (longitude of 60.5°E) also revealed a very similar structure as well. Their study shows that the coastal region is underlain by a very thick low-Vs (<3.3 km/s) sedimentary cover in excess of 22 km. Moreover, Kaviani et al. (2020) reported a very low velocities to 20 km depth beneath the Makran. In the coastal Makran, Motaghi et al. (2020) suggested that the base of the accretionary wedge is gently deepening from 9 to 15 km within a 60 km distance of the shoreline. Penney et al. (2017) found the sedimentary section to be ~26 km thick in the same region. An active-source seismic survey from the coastline to the southern Jazmurian Depression by Haberland et al. (2020) estimated a maximum thickness of ~35 km for the accretionary wedge. In the most recent studies, Irandoust et al. (2022) found very thick low velocity from coastal Makran and the thickness has been reduced to south of Jazmurian.

We found a moho depth in the coastal region of around 40 km. Previous studies suggest a crustal thickness of ~20–33 km for the coastal Makran (Abdetedal et al., 2015; Abdollahi et al., 2018) but most recent reports by Priestley et al. (2022), Kaviani et al. (2020) and Irandoust et al. (2022) report moho depth beneath coastal Makran to south of Jazmurian of 35 km to slightly more than 40 km. Based on Irandoust et al. (2022), near the Zagros-Makran boundary, where the transition from continental Zagros to oceanic Makran occurs, the Moho is at >40 km depth. Our Moho map shows that from the coastal Makran to Jazmurian the moho is relatively flat and confirms the recent studies with a depth of ~ 42 km.

Jazmurian Depression

The Jazmurian Depression is situated above the makran subduction zone (Farhoudi & Karig, 1997; McCall, 1997) and sits between a volcanic arc in the north and an accretionary prism in the south. The Vs structure of the depression in our profile shows velocities higher than the neighboring regions to the south and north. The depth of low Vs < 3.3 km/s related to sedimentary has slightly decreases, which indicates that the sediment cover of the basin is rather thin. Based on our knowledge of slab geometry east of the Jazmurian (Priestley et al., 2022), we expect the subducting plate to have a shallow dip beneath the Jazmurian as well, and we interpret the interface shown between 40 and 45 km in profile CC' to be the base of the subducting oceanic crust. Mokhtarzadeh et al. (2025), Irandoust et al. (2022) and Kaviani et al. (2020) reported a flat moho beneath Jazmurian with depth of 40 to 47 km. While Priestley et al. (2022), Abdetedal et al., 2015, Shad Manaman et al. (2011) and Abdollahi et al. (2019) estimated a Moho depth of in range of 37 to around 45 km. Mokhtarzadeh et al. (2025)

Volcanic Arc

The depth of low velocity in the upper crust of the volcanic arc is similar to that of the Jazmurian depression. A sharp northward increase in Moho depth beneath the Makran highlands signals the onset of underthrusting of the Arabian oceanic crust beneath the Iranian plateau. The steepening of the Moho reaches its peak depth (~55 km) as the subducting plate bends beneath the Taftan-Bazman volcanic arc. The deepest portion of the Moho is concentrated near the Taftan volcano. Previous studies have reported thickening in this region, although with shallower depths than those observed in our findings. Earlier research near this profile such as Abdetedal et al. (2015) estimated Moho depths more than 50 km. Also, other studies (Kaviani et al., 2020; Irandoust et al., 2022) reported similar moho depth range. Priestely et al. (2022) was unable pinpoint the moho depth beneath the volcanic arc but they estimate it to be ~ 60 km.

Lut Block

Lut block, a stable and relatively aseismic block is surrounded by active fault systems. This area is characterized by mostly flat terrain with altitudes below a kilometer. Given the direct relationship of the lowest shear velocities in the upper crust with sedimentary basins, the Vs maps show regions of thick sediments in central Iran and the Lut Block.

Within the Lut Block, the crustal thickness varies smoothly from ~40 km in the central and northeastern part to ~50 km in the southern end of the microplate. Our finding has good agreement with previous studies. A recent S-wave receiver function study by Wu et al. (2021) in eastern Iran revealed a Moho 35–40 km below the central and northern parts of the Lut and a slightly deeper Moho 40–45 km below the northern Sistan Suture Zone. Kaviani et al. (2020), Irandoust et al. (2022), and Abdetedal. (2015) all also reported relatively flat crustal thicknesses ranging from about 35 to 45 km in this region.

Low velocity in Lut magmatic belt with low-Q_{Lg} and low-Q_{Pn} values suggests magmatic accumulations in the crust and uppermost mantle (e.g., Amini et al., 2012; Hearn, 2022; Kaviani et al., 2022; Pei et al., 2011; Yang et al., 2023b). We can see two intense low velocities in upper crust and upper mantle (400 to 450 km and 850 km) which may confirm attenuation results.

The end of this profile, which is beneath the Doruneh fault, coincides with the end of profile BB' (Binalud) and the low velocity in upper crust is similarly related to sedimentary layer obtained by magnetic study by Mousavi and Ebbing (2018) which is confirmed by Yang et al. (2023b) is very low-quality factor (< 200) beneath this area.

5.3.2 Uppermost Mantle

The shear wave velocity images of the upper-mantle beneath the Makran subduction zone reveal a high-velocity anomaly beneath the Oman seafloor, which is subducting beneath the entire Makran belt. This high-velocity zone is indicative of a low-angle subduction zone (Yaminifard et al. 2007), suggesting relatively shallow crustal thickness in this area (Yaminifard & Hatzfeld 2008). In contrast, the lower crust beneath the forearc, volcanic arc, and back arc regions of the Makran subduction zone is characterized by low-velocity structures. Our findings indicate that the high-velocity slab of the Arabian plate subducts northward beneath the low-velocity overriding lithosphere of the Lut block in western Makran. The slab in this region begins with a gentle dip and steepens as it descends into the asthenosphere beneath the volcanic arc, consistent with the results of Zarifi (2006) and Shad Manaman et al. (2011). Further north along the profile, our velocity map shows a low-velocity uppermost mantle beneath the northeast of Lut block (L2). This low velocity immediately below the crust in our image may suggest that the upper mantle beneath the Lut Block is hotter

than the surrounding regions. This low-velocity coincides with strong attenuation seen by Yang et al. (2023a and b).
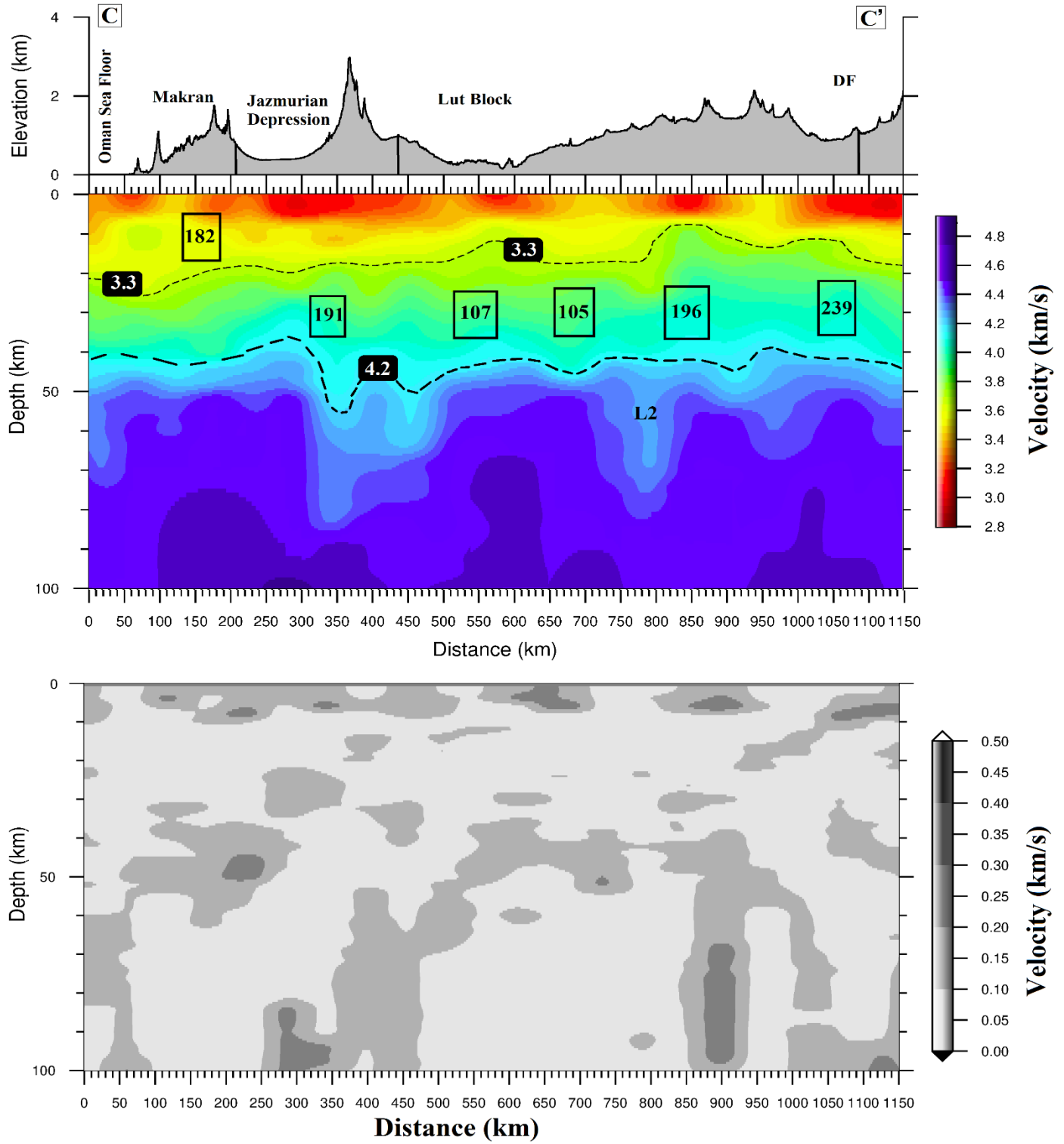

Figure 18. Transect along profile CC′ show shear wave velocities (top) and their associated uncertainties (bottom). The locations of the profiles are given in Figure 1.

5.4 Profile DD'

This horizontal profile extends from the center to the eastern edge of the model. According to Fig. 3, the starting point of the profile corresponds to an area with one of the strongest ray coverages, while the endpoint lies in a region with the weakest coverage. Consequently, we expect the highest lateral resolution at the start and the lowest at the end of the profile. As anticipated, the resolution length is low at the beginning of the profile but increases significantly toward the eastern edge of the model. In this profile, the highest uncertainties are mostly concentrated in the deeper structures, whereas in the shallow layers, uncertainties remain below 0.2 km/s.

5.4.1 Crust and to Moho

This profile extends through southeast Urumieh-Dokhtar, Central Iran, the Lut Block, and the Sistan Suture Zone (Fig. 18). Low shear wave velocities (lower than 3.3 km/s) in the upper crust are associated with sedimentary layers extending from depth of around 12 km beneath Urumieh-Dokhtar to below than 10 km beneath central Iran, Lut block and Sistan suture zone. Shear-wave velocity in central Iran is laterally more or less constant, especially in the lower crust. This relatively uniform lower crust may reflect a strong and coherent lithospheric structure. Such seismic characteristics, together with the limited internal deformation and concentrated seismicity along major strike-slip faults, support the interpretation of eastern Iran behaving as a rigid block system, as proposed by Walpersdorf et al. (2014).

The Sistan Zone, which is situated between the Lut and Helmand Blocks in Pakistan, was once part of the back-arc domain of the Neo-Tethys Ocean. According to our shear wave velocity maps, the Sistan Zone predominantly exhibits lower velocities in both the crust and sub-crustal regions. The eastern portion of the zone shows particularly low velocities, likely due to its position over the mantle wedge of the Makran Subduction Zone.

5.4.2 Uppermost Mantle

Relatively low velocity zone beneath Urumieh-Dokhtar supported by McKenzie and Priestley (2016). They analyzed magma compositions in this area and estimated a negative density contrast of -60 kg/m³ between the convecting upper mantle and the upper mantle source regions of the magmas, attributing this contrast to purely compositional variations. More recently, Yang et al. (2023a, b) confirmed the presence of this low-velocity zone, reporting strong attenuation in the southeast of the UDMA associated with younger magmatism

The shear-wave velocity images beneath the Lut block show a high-velocity anomaly interpreted as the subducting Arabian plate. It should be noted that profile DD′ is not perfectly aligned with the strike of the Arabian plate, which moves almost northward toward Central Iran. Consequently, the high-velocity feature observed along this profile likely represents a portion of the northern edge of the slab intersecting the profile, rather than the full thickness of the subducting plate. The anomaly in profile DD′ should be considered as an approximate representation of the slab's position.

In eastern Iran, beneath the northern end of the Sistan Zone, both the crust and the uppermost mantle (L2) exhibit low shear-wave velocities (Vs). Based on S receiver function measurements and waveform modeling along a seismic array in eastern Iran, Wu et al. (2021) estimated more than a 4% drop in shear-wave velocity across the lithosphere-asthenosphere boundary (LAB), at the northern end of the Sistan Suture. This velocity drop likely reflects partial melting in the mantle, with melt migrating upward into the overlying crust and consequently reducing crustal Vs a pattern comparable to that observed in the crust and uppermost mantle of the Makran Volcanic Belt (Priestley et al., 2022). Yang et al. (2023a and b) in their uppermost mantle

maps clearly reported a sequence of relatively low and high attenuations from Lut block to Sistan suture zone, respectively.
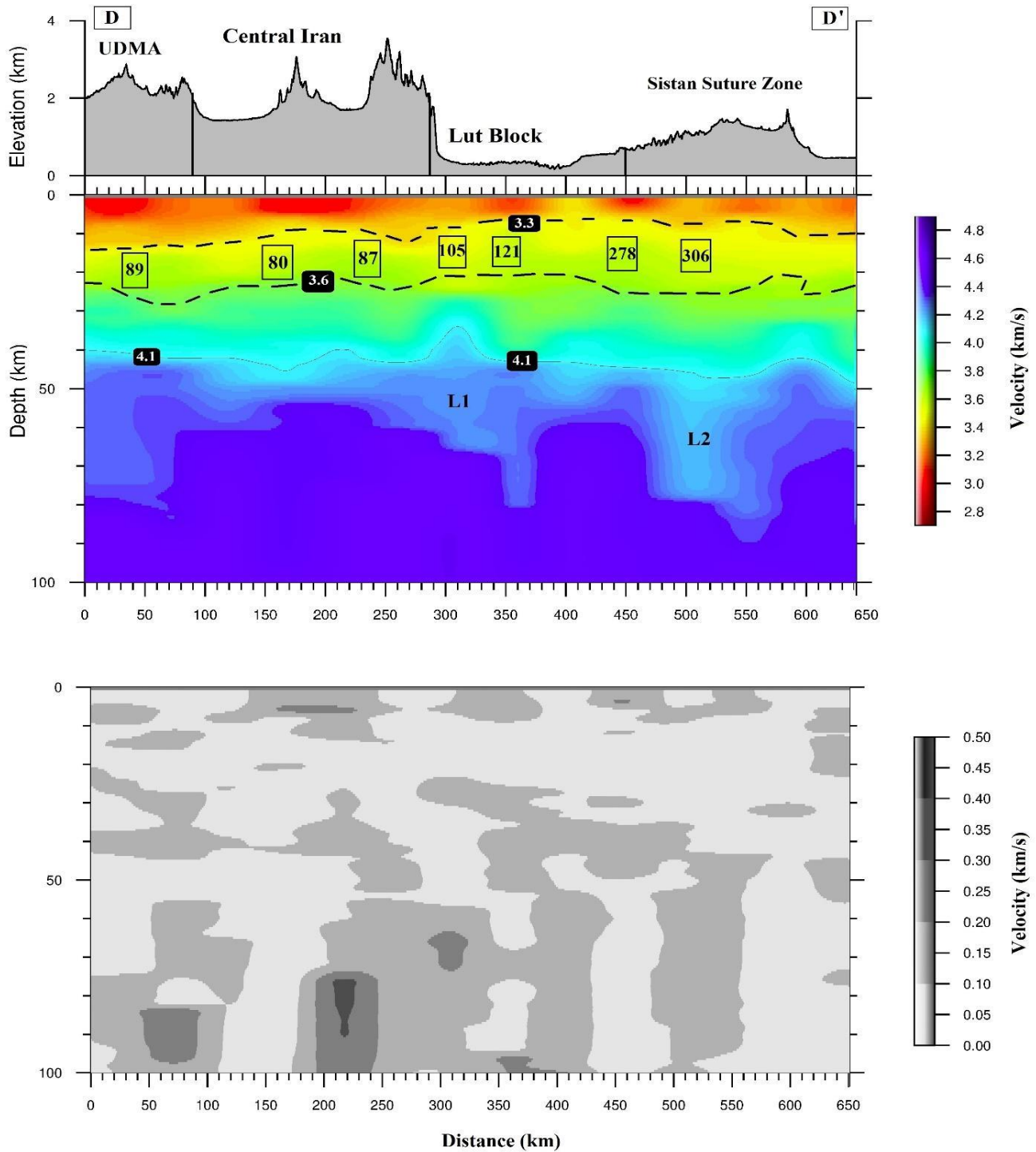

Figure 19. Transect along profile DD′ show shear wave velocities (top) and their associated uncertainties (bottom). The locations of the profiles are given in Figure 1.

6 CONCLUSSION

We assembled a comprehensive dataset of Rayleigh wave group velocity measurements derived from ambient noise cross-correlations and regional earthquakes across the Iranian Plateau. Using this dataset, we produced group velocity maps with two tomographic techniques: the Fast-Marching Method (Rawlinson and Sambridge, 2005) and the SOLA Backus–Gilbert approach (Zaroli, 2016), allowing us to access both linear and non-linear inversion frameworks for improved interpretation, as discussed in Amiri et al. (2023).

The resolution and uncertainty estimates provided by the SOLA inversion enabled us to introduce a homogenization step prior to performing a Bayesian Markov Chain Monte Carlo (MCMC) inversion. This step was critical for ensuring that the resolution across all periods was consistent and meaningful, and it helped avoid biases that could arise from varying lateral resolutions and inconsistent uncertainty estimates across the dataset. Specifically, without homogenization, regions with poor path coverage would be unduly weighted during inversion, leading to inaccurate or skewed Vs models. The homogenization process corrected this, standardizing resolution at each point and enabling a more reliable 3D shear-wave velocity model.

We plotted four shear wave velocity cross-sections, along with their corresponding uncertainties down to a depth of 100 km, perpendicular to key geological regions across the Iranian Plateau. Our results confirm the effectiveness of the SOLA method in generating unbiased tomographic models with quantifiable resolution and uncertainty particularly valuable in tectonically complex and data-limited regions. The resulting 3D Vs model reveals pronounced lateral and vertical heterogeneities shaped by the Arabia–Eurasia continental collision, including crustal thickening beneath the Sanandaj Sirjan Zone and thinning beneath Central Iran. The presence of the asthenospheric upwelling, especially in the southwestern part of the Central Iran, at a depth of subcrustal lithosphere. Low-velocity anomalies are associated with sedimentary basins, volcanic arcs, and potential asthenospheric upwellings, offering key insights into the ongoing geodynamic processes within the plateau.

This study not only improves our understanding of the lithospheric structure of the Iranian Plateau but also provides a robust methodological framework for future seismic imaging studies in other tectonically active regions.

Declaration of interests

The authors declare that they have no known competing financial interests or personal relationships that could have appeared to influence the work reported in this paper.

Acknowledgements

References

Abbassi, A., Nasrabadi, A., Tatar, M., Yaminifard, F., Abbassi, M.R., Hatzfeld, D., Priestley, K., 2010. Crustal velocity structure in the southern edge of the Central Alborz (Iran). *J. Geodyn.* 49(2), 68–78. https://doi.org/10.1016/j.jog.2009.09.044.

Abdetedal, M., Shomali, Z.H., Gheitanchi, M.R., 2015. Ambient noise surface wave tomography of the Makran subduction zone, south-east Iran: Implications for crustal and uppermost mantle structures. *Earthquake Sci.* 28(4), 235–251. https://doi.org/10.1007/s11589-015-0132-1.

Abdollahi, S., Zeyen, H., Ardestani, V.E., Shomali, Z.H., 2019. 3D joint inversion of gravity data and Rayleigh wave group velocities to resolve shear-wave velocity and density structure in the Makran subduction zone, south-east Iran. *J. Asian Earth Sci.* 173, 275–290. https://doi.org/10.1016/j.jseaes.2019.01.029.

Aflaki, M., Mousavi, Z., Ghods, A., Shabanian, E., Vajedian, S., Akbarzadeh, M., 2019. The 2017 Mw 6 Sefid Sang earthquake and its implication for the geodynamics of NE Iran. *Geophys. J. Int.* 218(2), 1227–1245. https://doi.org/10.1093/gji/ggz172.

Afshar-Harb, A., 1979. The stratigraphy, tectonics and petroleum geology of the Kopet Dagh region, northeastern Iran. PhD thesis. Petroleum Geology Section, Royal School of Mines, Imperial College of Science and Technology.

Afonso, J., Fullea, J., Griffin, W., Yang, Y., Jones, A., Connolly, J., O'Reilly, S., 2013. 3-D multiobservable probabilistic inversion for the compositional and thermal structure of the lithosphere and upper mantle. I: A priori petrological information and geophysical observables. *J. Geophys. Res. Solid Earth* 118, 2586–2617. https://doi.org/10.1002/jgrb.50124.

Aftabi, A., Atapour, H., 2000. Regional aspects of shoshonitic volcanism in Iran. *Episodes* 23, 119–125.

Agard, P., Omrani, J., Jolivet, L., Whitechurch, H., Vrielynck, B., Spakman, W., Monie, P., Meyer, B., Wortel, R., 2011. Zagros orogeny: a subduction-dominated process. *Geol. Mag.* 148(5–6), 692–725. https://doi.org/10.1017/S001675681100046X.

Ahmadzadeh, S., Parolai, S., Javan-Doloei, G., Oth, A., 2017. Attenuation characteristics, source parameters and site effects from inversion of S waves of the March 31, 2006 Silakhor aftershocks. *Ann. Geophys.* 60, 668.

Alavi, M., 1992. Thrust tectonics of the Binalood region, NE Iran. *Tectonics* 11(2), 360–370. https://doi.org/10.1029/91TC02217.

Alavi, M., 1994. Tectonics of the Zagros orogenic belt of Iran: New data and interpretations. *Tectonophysics* 229, 211–238.

Al-Damegh, K., Sandvol, E., Al-Lazki, A., Barazangi, M., 2004. Regional seismic wave propagation (Lg and Sn) and Pn attenuation in the Arabia plate and surrounding regions. *Geophys. J. Int.* 157(2), 775–795.

Allen, M., Jackson, J.A., Walker, R., 2004. Late Cenozoic reorganization of the Arabia–Eurasia collision and the comparison of short-term and long term deforma tion rates. Tectonics 23 (2). https://doi.org/10.1029/2003TC001530.

Al-Lazki, A.I., Seber, D., Sandvol, E., Turkelli, N., Mohamad, R., Barazangi, M., 2003. Tomographic Pn velocity and anisotropy structure beneath the Anatolian plateau (eastern Turkey) and the surrounding regions. *Geophys. Res. Lett.* 30(24), 8043.

Al-Lazki, A.I., Sandvol, E., Seber, D., Barazangi, M., Turkelli, N., Mohamad, R., 2004. Pn tomographic imaging of mantle lid velocity and anisotropy at the junction of the Arabian, Eurasian and African plates. *Geophys. J. Int.* 158, 1024–1040.

Al-Lazki, A.I., Al-Damegh, K.S., El-Hadidy, S.Y., Ghods, A., Tatar, M., 2014. Pn-velocity structure beneath Arabia–Eurasia Zagros collision and Makran subduction zones. *Geol. Soc. Lond., Spec. Publ.* 392(1), 45–60. https://doi.org/10.1144/SP392.3.

Amini, S., Shomali, Z., Koyi, H., Roberts, R., 2012. Tomographic upper-mantle velocity structure beneath the Iranian Plateau. *Tectonophysics*. https://doi.org/10.1016/j.tecto.2012.06.009.

Amiri, S., Maggi, A., Tatar, M., Zigone, D., Zaroli, C., 2023. Rayleigh wave group velocities in North-West Iran: SOLA Backus-Gilbert vs. Fast Marching tomographic methods. *Seismica* 2. https://doi:10.26443/seismica.v2i2.1011

Backus, G.E., Gilbert, F., 1967. Numerical Applications of a Formalism for Geophysical Inverse Problems. *Geophys. J. Int.* 13(1–3), 247–276. https://doi.org/10.1111/j.1365-246X.1967.tb02159.x.

Backus, G.E., Gilbert, F., 1968. The Resolving Power of Gross Earth Data. *Geophys. J. Int.* 16(2), 169–205. https://doi.org/10.1111/j.1365-246X.1968.tb00216.x.

Backus, G., Gilbert, F., 1970. Uniqueness in the inversion of inaccurate gross Earth data. *Phil. Trans. R. Soc. A* 266(1173), 123–192.

Bensen, G.D., Ritzwoller, M.H., Barmin, M.P., Levshin, A.L., Lin, F., Moschetti, M.P., Shapiro, N.M., Yang, Y., 2007. Processing seismic ambient noise data to obtain reliable broad-band surface wave dispersion measurements. *Geophys. J. Int.* 169, 1239–1260. https://doi.org/10.1111/j.1365-246X.2007.03374.x.

Berteussen, K.-A., 1977. Moho depth determinations based on spectral-ratio analysis of NORSAR long-period P waves. *Phys. Earth Planet. Inter.* 15, 13–27.

Byrne, D.E., Sykes, L.R., Davis, D.M., 1992. Great thrust earthquakes and aseismic slip along the plate boundary of the Makran Subduction Zone. *J. Geophys. Res.* 97(B1), 449–478.

Chiu, H.-Y., Chung, S.-L., Zarrinkoub, M.H., Mohammadi, S.S., Khatib, M.M., Iizuka, Y., 2013. Zircon U–Pb age constraints from Iran on the magmatic evolution related to Neotethyan subduction and Zagros orogeny. *Lithos* 162–163, 70–87.

Delph, J.R., et al., 2017. The effects of subduction termination on the continental lithosphere: Linking volcanism, deformation, surface uplift, and slab tearing in central Anatolia. *Geosphere* 13, 1788–1805.

Fard, R. A., Doloei, G. J., Rahimi, H., & Farrokhi, M. (2019). Attenuation of P and S waves in Western part of Iran. *Geophysical Journal International, 218*, 1143–1156. https://doi.org/10.1093/gji/ggz239

Gallagher, K., Charvin, K., Nielsen, S., Sambridge, M., & Stephenson, J. (2009). Markov chain Monte Carlo (MCMC) sampling methods to determine optimal models, model resolution and model choice for Earth Science problems. *Marine and Petroleum Geology, 26*, 525–535. https://doi.org/10.1016/j.marpetgeo.2009.01.003

Goes, S., Govers, R., & Vacher, P. (2000). Shallow mantle temperatures under Europe from P and S wave tomography. *Journal of Geophysical Research, 105*(B11), 15,153–15,169. https://doi.org/10.1029/2000JB900139

Golonka, Jan (2004). Plate tectonic evolution of the southern margin of Eurasia in the Mesozoic and Cenozoic. *Tectonophysics*, 381(1–4): 235-273. DOI: 10.1016/j.tecto.2002.06.004

Guo, Z., Yang, Y., & Chen, Y. J. (2016). Crustal radial anisotropy in Northeast China and its implications for the regional tectonic extension. *Geophysical Journal International, 207*, 197–208. https://doi.org/10.1093/gji/ggw272

Haberland, C., Mokhtari, M., Babaei, H. A., Ryberg, T., Masoodi, M., Partabian, A., & Lauterjung, J. (2020). Anatomy of a crustal-scale accretionary complex: Insights from deep seismic sounding of the onshore western Makran subduction zone, Iran. *Geology, 49*(1), 3–7. https://doi.org/10.1130/G47700.1

Hafkenscheid, E., Wortel, M., & Spakman, W. (2006). Subduction history of the Tethyan region derived from seismic tomography and tectonic reconstructions. *Journal of Geophysical Research, 111*. https://doi.org/10.1029/2005JB003791

Hatzfeld, D., & Molnar, P. (2010). Comparisons of the kinematics and deep structures of the Zagros and Himalaya and of the Iranian and Tibetan plateaus and geodynamic implications. *Reviews of Geophysics, 48*. https://doi.org/10.1029/2009RG000304.

Hatzfeld, D., Tatar, M., Priestley, K. & Ghafory-Ashtiany, M., 2003. The crustal velocity structure beneath the Zagros Mountain belt (Iran), Geophys. J. Int., 156, 2, 255–266. https://doi.org/10.1111/j.1365-246X.2003.02145.x

Hearn, T. M. (2022). Two-dimensional attenuation and velocity tomography of Iran. *Geosciences, 12*(11), 397. https://doi.org/10.3390/geosciences12110397

Hessami, K., Koyi, H., Talbot, C. J., Tabasi, H., and Shabanian, E., (2001). Progressive unconformities within and evolving foreland fold-thrust belt, Zagros Mountains, J. Geol. Soc. London, 158, 969-981.

Hessami, K., Nilforoushan, F., and Talbot, C., (2006), Active deformation within the Zagros Mountains deduced from GPS measurements, J. Geol. Soc. London, 163, 143-148.

Hollingsworth, J., Fattahi, M., Walker, R., Talebian, M., Bahroudi, A., Bolourchi, M. J., et al. (2010). Oroclinal bending, distributed thrust and strike-slip faulting, and the accommodation of Arabia–Eurasia convergence in NE Iran since the Oligocene. *Geophysical Journal International, 181*(3), 1214–1246. https://doi.org/10.1111/j.1365-246X.2010.04591.x

Hammond, W. C., & Humphreys, E. D. (2000). Upper-mantle seismic wave velocity: Effects of realistic partial melt geometries. *Journal of Geophysical Research, 105*(B5), 10975–10986. https://doi.org/10.1029/1999JB900434

Irandoust, M. A., Sobouti, F., & Rahimi, H. (2016). Lateral and depth variations of coda Q in the Zagros region of Iran. *Journal of Seismology*, 20(1), 197–211. https://doi.org/10.1007/s10950-015-9520-1

Irandoust, M. A., Priestley, K., & Sobouti, F. (2022a). High-resolution lithospheric structure of the Zagros collision zone and Iranian plateau. *Journal of Geophysical Research: Solid Earth, 127*(11), e2022JB025009. https://doi.org/10.1029/2022JB025009

Jackson, J., & Fitch, T. J. (1981). Basement faulting and the focal depths of the larger earthquakes in the Zagros mountains (Iran). *Geophysical Journal International, 64*(3), 561–586. https://doi.org/10.1111/j.1365-246X.1981.tb02685.x

Jackson, J., & McKenzie, D. (1984). Active tectonics of the Alpine—Himalayan Belt between western Turkey and Pakistan. Geophysical Journal International, 77(1), 185–264. https://doi.org/10.1111/j.1365-246X.1984.tb01931.x

Jentzer, M., Fournier, M., Agard, P., Omrani, J., Khatib, M. M., & Whitechurch, H. (2017). Neogene to Present paleostress field in Eastern Iran (Sistan belt) and implications for regional geodynamics. *Tectonics, 36*(2), 321–339. https://doi.org/10.1002/2016TC004275

Kaviani, A., et al. (2020). Crustal and uppermost mantle shear wave velocity structure beneath the Middle East from surface wave tomography. *Geophysical Journal International, 222*(2), 1349–1365. https://doi.org/10.1093/gji/ggaa075

Kennett, B., Sambridge, M., and Williamson, P. R. Subspace methods for large inverse problems with multiple parameter classes. (1988). *Geophysical Journal International*, 94(2):237–247. doi:10.1111/j.1365-246x.1988.tb05898.x.

Khorrami, F., Vernant, P., Masson, F., Nilfouroushan, F., Mousavi, Z., Nankali, H., et al. (2019). An up-to-date crustal deformation map of Iran using integrated campaign-mode and permanent GPS velocities. *Geophysical Journal International, 217*(2), 832–843. https://doi.org/10.1093/gji/ggz045

Koulakov, I. (2011). High-frequency P and S velocity anomalies in the upper mantle beneath Asia from inversion of worldwide traveltime data. Journal of Geophysical Research, 116(B4), B04301. https://doi.org/10.1029/2010JB007938

Kreemer, C., Blewitt, G., & Klein, E. C. (2014). A geodetic plate motion and Global Strain Rate Model. *Geochemistry, Geophysics, Geosystems, 15*(10), 3849–3889. https://doi.org/10.1002/2014GC005407

Latallerie, F., Zaroli, C., Lambotte, S., & Maggi, A. (2022). Analysis of tomographic models using resolution and uncertainties: A surface wave example from the Pacific. *Geophysical Journal International, 230*(2), 893–907. https://doi.org/10.1093/gji/ggac072

Lehujeur, M., Vergne, J., Schmittbuhl, J., Zigone, D., Le Chenadec, A., & EstOF Team. (2018). Reservoir imaging using ambient noise correlation from a dense seismic network. *Journal of Geophysical Research: Solid Earth, 123*. https://doi.org/10.1029/2018JB015440

Lin, F.-C., Moschetti, M.P. & Ritzwoller, M.H., (2008). Surface wave tomog raphy of the western United States from ambient seismic noise: Rayleigh and Love wave phase velocity maps, *Geophys. J. Int.*, 173, 281–298.

Lyberis, N., & Manby, G. (1999). Oblique to orthogonal convergence across the Turan block in the post-Miocene. *AAPG Bulletin, 83*(7), 1135–1160. https://doi.org/10.1306/E4FD2E97-1732-11D7-8645000102C1865D

Maggi, A., & Priestley, K. (2005). Surface waveform tomography of the Turkish–Iranian plateau. *Geophysical Journal International, 160*, 1068–1080. https://doi.org/10.1111/j.1365-246X.2005.02526.x

Maheri-Peyrov, M., Ghods, A., Abbasi, M., Bergman, E., & Sobouti, F. (2016). ML shear wave velocity tomography for the Iranian Plateau. *Geophysical Journal International, 205*(1), 179–191. https://doi.org/10.1093/gji/ggv504

Mahmoodabadi, M., Yaminifard, F., Tatar, M., & Kaviani, A. (2020). Shear wave velocity structure of the upper-mantle beneath the northern Zagros collision zone revealed by nonlinear teleseismic tomography and Bayesian Monte-Carlo joint inversion of surface wave dispersion and teleseismic P-wave coda. *Physics of the Earth and Planetary Interiors, 300*, 106444. https://doi.org/10.1016/j.pepi.2019.106444

Manaman, N. S., & Shomali, H. (2010). Upper mantle S-velocity structure and Moho depth variations across Zagros belt, Arabian–Eurasian plate boundary. *Physics of the Earth and Planetary Interiors, 180*(1–2), 92–103. https://doi.org/10.1016/j.pepi.2009.12.009

Martin, H., Smithies, R.H., Rapp, R., Moyen, J.-F., & Champion, D. (2005). An overview of adakite, tonalite–trondhjemite–granodiorite (TTG), and sanukitoid: relationships and some implications for crustal evolution. *Lithos, 79*(1–2), 1–24. https://doi.org/10.1016/j.lithos.2004.04.048

McCall, G. J. H. (1997). The geotectonic history of the Makran and adjacent areas of southern Iran. *Journal of Asian Earth Sciences, 15*(6), 517–531. https://doi.org/10.1016/S0743-9547(97)00032-9

McKenzie, D., & Priestley, K. (2016). Speculations on the formation of cratons and cratonic basins. *Earth and Planetary Science Letters, 435*, 94–104. https://doi.org/10.1016/j.epsl.2015.12.010

Moghaddam, M. J., Karimpour, M. H., Shafaroudi, A. M., Santos, J. F., & Corfu, F. (2021). Middle Eocene magmatism in the Khur region (Lut Block, Eastern Iran): Implications for petrogenesis and tectonic setting. *International Geology Review, 63*(9), 1051–1066. https://doi.org/10.1080/00206814.2019.1708815

Mokhtarzadeh, R., Sobouti, F., and Keith Priestley, K., (2025). Imaging the seismic structure of the western Makran Subduction Zone. *Geophysical Journal International*, 242, 1–16, https://doi.org/10.1093/gji/ggaf196

Mohammadi, E., Sodoudi, F., Kind, R., & Rezapour, M. (2013). Presence of a layered lithosphere beneath the Zagros collision zone. *Tectonophysics, 608*, 366–375. https://doi.org/10.1016/j.tecto.2013.09.017

Mohammadi, N., Sodoudi, F., Mohammadi, E., & Sadidkhouy, A. (2013). New constraints on lithospheric thickness of the Iranian plateau using converted waves. *Journal of Seismology, 17*(3), 883–895. https://doi.org/10.1007/s10950-013-9359-2

Molinaro, M., Guezou, J. C., Leturmy, P., Eshraghi, S. A., & de Lamotte, D. F. (2004). The origin of changes in structural style across the Bandar Abbas syntaxis, SE Zagros (Iran). *Marine and Petroleum Geology*, 21(6), 735–752. https://doi.org/10.1016/j.marpetgeo.2004.04.001

Mortezanejad, G., Rahimi, H., Romanelli, F., & Panza, G. F. (2018). Lateral variation of crust and upper mantle structures in NW Iran derived from surface wave analysis. *Journal of Seismology, 23*(1), 77–108. https://doi.org/10.1007/s10950-018-9794-1

Morley, C. K., Kongwung, B., Julapour, A. A., Abdolghafourian, M., Hajian, M., Waples, D., et al. (2009). Structural development of a major late Cenozoic basin and transpressional belt in central Iran: The Central Basin in the Qom-Saveh area. *Geosphere, 5*(4), 325–362. https://doi.org/10.1130/GES00223.1

Mosegaard, K., & Sambridge, M. (2002). Monte Carlo analysis of inverse problems. *Inverse Problems, 18*(2), R29–R54. https://doi.org/10.1088/0266-5611/18/2/201

Mottaghi, A., Rezapour, M., & Kom, M. (2013). Ambient noise surface wave tomography of the Iranian Plateau. *Geophysical Journal International, 193*(1), 452–462. https://doi.org/10.1093/gji/ggs103

Motaghi, K., Tatar, M., and Priestley, K., 2012. Crustal thickness variation across the northeast Iran continental collision zone from teleseismic converted waves. J Seismol., DOI 10.1007/s10950-011-9267-2.

Motaghi, K., Tatar, M., Priestley, K., Romanelli, F., Doglioni, C., & Panza, G. F., (2015). The deep structure of the Iranian Plateau. Gondwana Research, 28(1), 407–418.

Motaghi, K., Shabanian, E., Tatar, M., Cuffaro, M., Doglioni, C., (2017a). The south Zagros suture zone in teleseismic images. Tectonophysics, 694, 292-301.

Motaghi, K., Shabanian, E., Kalvandi, F., (2017b). Underplating along the northern portion of the Zagros suture zone, Iran. *Geophysical Journal International*, 210 (1), 375–389

Motaghi, K., Ghods, A., Sobouti, F., Shabanian, E., Mahmoudabadi, M. & Priestley, K., 2018. Lithospheric seismic structure of the West Alborz–Talesh ranges, Iran, *Geophysical Journal International*, 215, 1766-1780.

Motaghi, Kh., Shabanian, E., and Nozad-Khalil, T., (2020). Deep structure of the western coast of the Makran subduction zone, SE Iran. *Tectonophysics*, 776.

Movaghari, R. and Doloei, G. J. 3-D crustal structure of the Iran plateau using phase velocity ambient noise tomography. Geophysical Journal International, 220:1555–1568, 2019. doi: 10.1093/gji/ggz537.

Movaghari, R., Doloei, G., Yang, Y., Tatar, M., and Sadidkhouy, A. Crustal Radial Anisotropy of the Iranian Plateau Inferred from Ambient Noise Tomography. Journal of Geophysical Research: Solid Earth, 126, 2021. doi: 10.1029/2020jb020236.

Omrani, J., et al. (2008). Arc-magmatism and subduction history beneath the Zagros Mountains, Iran: A new report of adakites and geodynamic consequences. *Lithos*, 106(3), 380–398.

Paige, C. and Saunders, M. LSQR: An Algorithm for Sparse Linear Equations and Sparse Least Squares. *ACM Trans actions on Mathematical Software*. (1982). 8(1):43–71. 10.1145/355984.355989.

Pang, K.-N., Chung, S.-L., Zarrinkoub, M. H., Khatib, M. M., Mohammadi, S. S., Chiu, H.-Y., et al. (2013). Eocene–Oligocene post-collisional magmatism in the Lut–Sistan region, eastern Iran: Magma genesis and tectonic implications. *Lithos*, 180–181, 234–251. https://doi.org/10.1016/j.lithos.2013.05.009

Paul, A., et al. (2006). Seismological evidence for crustal-scale thrusting in the Zagros Mountain belt (Iran). *Geophysical Journal International*, 166(1), 227–237.

Pedersen, H. A., Mars, J. I., & Amblard, P. O. (2003). Improving Surface Wave Group Velocity Measurements by Energy Reassignment. *Geophysics*, 68(2), 677–684. https://doi.org/10.1190/1.1567238

Pei, S., Sun, Y., & Nafi Toksöz, M. (2011). Tomographic Pn and Sn velocity beneath the continental collision zone from Alps to Himalaya. *Journal of Geophysical Research*, 116, B10311.

Penney, C., Tavakoli, F., Saadat, A., Nankali, H. R., Sedighi, M., Khorrami, F., et al. (2017). Megathrust and accretionary wedge properties and behaviour in the Makran subduction zone. *Geophysical Journal International*, 209(3), 1800–1830. https://doi.org/10.1093/gji/ggx126

Poli, P., Campillo, M., Pedersen, H., & the L.W. Group (2012). Body Wave Imaging of Earth's Mantle Discontinuities from Ambient Seismic Noise. *Science*, 338(6110), 1063–1065. https://doi.org/10.1126/science.1228194

Priestley, K., & McKenzie, D. (2006). The thermal structure of the lithosphere from shear wave velocities. *Earth and Planetary Science Letters*, 244, 285–301.

Priestley, K., Sobouti, F., Mokhtarzadeh, R., Irandoust, M., Ghods, R., Motaghi, K., & Ho, T. (2022). New constraints for the on-shore Makran Subduction Zone crustal structure. *Journal of Geophysical Research: Solid Earth*, 127(1), e2021JB022942. https://doi.org/10.1029/2021JB022942

Radjaee, A., Rham, D., Mokhtari, M., Tatar, M., Priestley, K., & Hatzfeld, D. (2010). Variation of Moho depth in the central part of the Alborz Mountains, northern Iran. *Geophysical Journal International*, 181(1), 173–184. https://doi.org/10.1111/j.1365-246X.2010.04518.x

Rastgoo, M., Rahimi, H., Motaghi, K., Shabanian, E., Romanelli, F., & Panza, G. F. (2018). Deep structure of the Alborz Mountains by joint inversion of P receiver functions and dispersion curves. Physics of the Earth and Planetary Interiors, 277, 70–80. https://doi.org/10.1016/j. pepi.2018.01.011

Rawlinson, N., & Sambridge, M. (2005). The fast marching method: an effective tool for tomographic imaging and tracking multiple phases in complex layered media. *Exploration Geophysics*, 36(4), 341–351. https://doi.org/10.1071/eg05341

Rawlinson, N., Fichtner, A., Sambridge, M., and Young, M. Seismic tomography and the assessment of uncertainty. (2014). *Advances in Geophysics*, 55:1–76. doi: 10.1016/bs.agph.2014.08.001.

Robert, A. M., Letouzey, J., Kavoosi, M. A., Sherkati, S., Müller, C., Vergés, J., & Aghababaei, A. (2014). Structural evolution of the Kopeh Dagh fold-and-thrust belt (NE Iran) and interactions with the South Caspian Sea Basin and Amu Darya Basin. *Marine and Petroleum Geology*, 57, 68–87. https://doi.org/10.1016/j.marpetgeo.2014.05.002

Salaün, G., Pedersen, H. A., Paul, A., Farra, V., Karabulut, H., Hatzfeld, D., et al. (2012). High-resolution surface wave tomography beneath the Aegean-Anatolia region: Constraints on upper-mantle structure. Geophysical Journal International, 190(1), 406–420. https://doi. org/10.1111/j.1365-246X.2012.05483.x

Saccani, E., Delavari, M., Beccaluva, L., & Amini, S. (2010). Petrological and geochemical constraints on the origin of the Nehbandan ophiolitic complex (eastern Iran): Implication for the evolution of the Sistan Ocean. *Lithos*, 117, 209–228.

Sambridge, M., Mosegaard, K., (2002). Monte Carlo methods in geophysical inverse pro blems. *Rev. Geophys*. 40 (3). https://doi.org/10.1029/2000RG000089.

Şengör, A. M. C., Altiner, D., Cin, A., Ustaömer, T., & Hsü, K. J. (1988). Origin and assembly of the Tethyside orogenic collage at the expense of Gondwana Land. In M. G. Audley-Charles & A. Hallam (Eds.), *Gondwana and Tethys* (Geological Society London Special Publication, Vol. 37, pp. 119–181). Geological Society of London. https://doi.org/10.1144/GSL.SP.1988.037.01.09

Shabanian, E., Bellier, O., Siame, L., Abbassi, M. R., Bourlès, D., Braucher, R., & Farbod, Y. (2012). The Binalud Mountains: A key piece for the geodynamic puzzle of NE Iran. *Tectonics*, 31(6), TC6003. https://doi.org/10.1029/2012TC00318

Shad Manaman, N., Shomali, H., & Koyi, H. (2011). New constraints on upper-mantle S-velocity structure and crustal thickness of the Iranian plateau using partitioned waveform inversion. *Geophysical Journal International*, 184(1), 247–267. https://doi.org/10.1111/j.1365-246X.2010.04822.x

Shafaii-Moghadam, H., & Stern, R. J. (2015). Ophiolites of Iran: Keys to understanding the tectonic evolution of SW Asia: (II) Mesozoic ophiolites. *Journal of Asian Earth Sciences*, 100, 31–59.

Shapiro, N. M., & Ritzwoller, M. H. (2002). Monte-Carlo inversion for a global shear-velocity model of the crust and upper mantle. *Geophysical Journal International*, 151(1), 88–105. https://doi.org/10.1046/j.1365-246X.2002.01742.x

Shen, W., Ritzwoller, M. H., Schulte-Pelkum, V., & Lin, F.-C. (2012). Joint inversion of surface wave dispersion and receiver functions: A Bayesian Monte-Carlo approach. *Geophysical Journal International*, 192, 807–836.

Sodoudi, F., Yuan, X., Kind, R., Heit, B., & Sadidkhouy, A. (2009). Evidence for a missing crustal root and a thin lithosphere beneath the Central Alborz by receiver function studies. *Geophysical Journal International*, 177(2), 733–742. https://doi.org/10.1111/j.1365-246X.2009.04115.x

Soffel, H. C., & Förster, H. G. (1984). Polar wander path of the Central-East-Iran Microplate including new results. *Neues Jahrbuch für Geologie und Paläontologie - Abhandlungen*, 168, 165–172. https://doi.org/10.1127/njgpa/168/1984/1

Stern, C. R., & Kilian, R. (1996). Role of the subducted slab, mantle wedge and continental crust in the generation of adakites from the austral volcanic zone. *Contributions to Mineralogy and Petrology*, 123, 263–281.

Stocklin, J. (1968). Structural history and tectonics of Iran: a review. *AAPG Bulletin*, 52, 1229–1258.

Stöcklin, J. (1974). Possible ancient continental margins in Iran. In The geology of continental margins (pp. 873–887). Springer. https://doi. org/10.1007/978-3-662-01141-6_64

Stoneley, R. (1990). The Arabian continental margin in Iran during the Late Cretaceous (Vol. 49, 787 795). Geological Society, London, Special Publications. https://doi.org/10.1144/GSL.SP.1992.049.01.48

Talebi, A., Medved, I., & Koulakov, I. (2025). Crustal structure of northwestern Iran on the basis of regional seismic tomography data. *Geosciences, 15*(2), 55. https://doi.org/10.3390/geosciences15020055

Talebian, M., & Jackson, J. (2004). A reappraisal of earthquake focal mechanisms and active shortening in the Zagros mountains of Iran. *Geophysical Journal International, 156*(3), 506–526.

Tatar, M., Hatzfeld, D., Martinod, J., Walpersdorf, A., Ghafori-Ashtiany, M., & Chéry, J. (2002). The present-day deformation of the central Zagros from GPS measurements. *Geophysical Research Letters, 29*(19), 33-1–33-4.

Tatar, M., Hatzfeld, D., & Ghafory-Ashtiany, M. (2004). Tectonics of the Central Zagros (Iran) deduced from microearthquake seismicity. *Geophysical Journal International, 156*(2), 255–266. https://doi.org/10.1111/j.1365-246X.2003.02145.x

Teknik, V., & Ghods, A. (2017). Depth of magnetic basement in Iran based on fractal spectral analysis of aeromagnetic data. *Geophysical Journal International, 209*(3), 1878–1891. https://doi.org/10.1093/gji/ggx132

Veisi, M., Sobouti, F., Chevrot, S., Abbasi, M., & Shabanian, E. (2021). Upper mantle structure under the Zagros collision zone; insights from 3D teleseismic P-wave tomography. *Tectonophysics*, 819, 229106. https://doi.org/10.1016/j.tecto.2021.229106

Vernant, P., Nilforoushan, F., Hatzfeld, D., Abbassi, M. R., Vigny, C., Masson, F., ... & Chéry, J. (2004). Present-day crustal deformation and plate kinematics in the Middle East constrained by GPS measurements in Iran and northern Oman. *Geophysical Journal International, 157*(1), 381–398.

Walpersdorf, A., Manighetti, I., Mousavi, Z., Tavakoli, F., Vergnolle, M., Jadidi, A., et al. (2014). Present-day kinematics and fault slip rates in eastern Iran, derived from 11 years of GPS data. *Journal of Geophysical Research: Solid Earth, 119*(2), 1359–1383. https://doi.org/10.1002/2013JB010620

Wu, Z., Chen, L., Talebian, M., Wang, X., Jiang, M., Ai, Y., et al. (2021). Lateral structural variation of the lithosphere-asthenosphere system in the northeastern to eastern Iranian plateau and its tectonic implications. *Journal of Geophysical Research: Solid Earth, 126*(1), e2020JB020256. https://doi.org/10.1029/2020JB020256

Yang, G., Chen, L., Zhao, L., Xie, X., & Yao, Z. (2023). Crustal Lg attenuation beneath the Iranian Plateau: Implications for Cenozoic magmatism related to slab subduction, slab break-off, and mantle flow. *Journal of Geophysical Research: Solid Earth, 128*(3). https://doi.org/10.1029/2022jb025664

Yang, G., Chen, L., Zhao, L., Xie, X., & Yao, Z. (2023). Segmented up-bending of the Arabian continental plate revealed by Pn attenuation tomography. *Journal of Geophysical Research: Solid Earth, 128*(3). https://doi.org/10.1029/2022jb025664

Yaminifard, F., Hatzfeld, D., Farahbod, A. M., Paul, A., & Mokhtari, M. (2007). The diffuse transition between the Zagros continental collision and the Makran oceanic subduction (Iran): Microearthquake seismicity and crustal structure. *Geophysical Journal International, 170*(1), 182–194. https://doi.org/10.1002/jgrb.50236

Yaminifard, F., & Hatzfeld, D. (2008). Seismic structure beneath Zagros-Makran transition zone (Iran) from teleseismic study: Seismological evidence for underthrusting and buckling of the Arabian plate beneath central Iran. *Journal of Seismology and Earthquake Engineering, 10*(1), 11–24. http://www.jsee.ir/article_240565.html

Zarifi, Z., & Atakan, K. (2006). The Makran subduction zone (Part I): Current state of crustal stress. *Bulletin of the Seismological Society of America (in review)*.

Zaroli, C. (2016). Global seismic tomography using Backus–Gilbert inversion. *Geophysical Journal International, 207*(2), 876–888. https://doi.org/10.1093/gji/ggw315

Zaroli, C., Koelemeijer, P., & Lambotte, S. (2017). Toward seeing the Earth's interior through unbiased tomographic lenses. *Geophysical Research Letters, 44*(17), 8700–8708. https://doi.org/10.1002/2017GL074996

Zaroli, C. (2019). Seismic tomography using parameter-free Backus–Gilbert inversion. *Geophysical Journal International, 218*(1), 619–630.

Zigone, D., Ben-Zion, Y., Campillo, M., & Roux, P. (2015). Seismic tomography of the Southern California plate boundary region from noise-based Rayleigh and Love waves. *Pure and Applied Geophysics, 172*(4), 1007–1032. https://doi.org/10.1007/s00024-014-0872-1

Supplementary
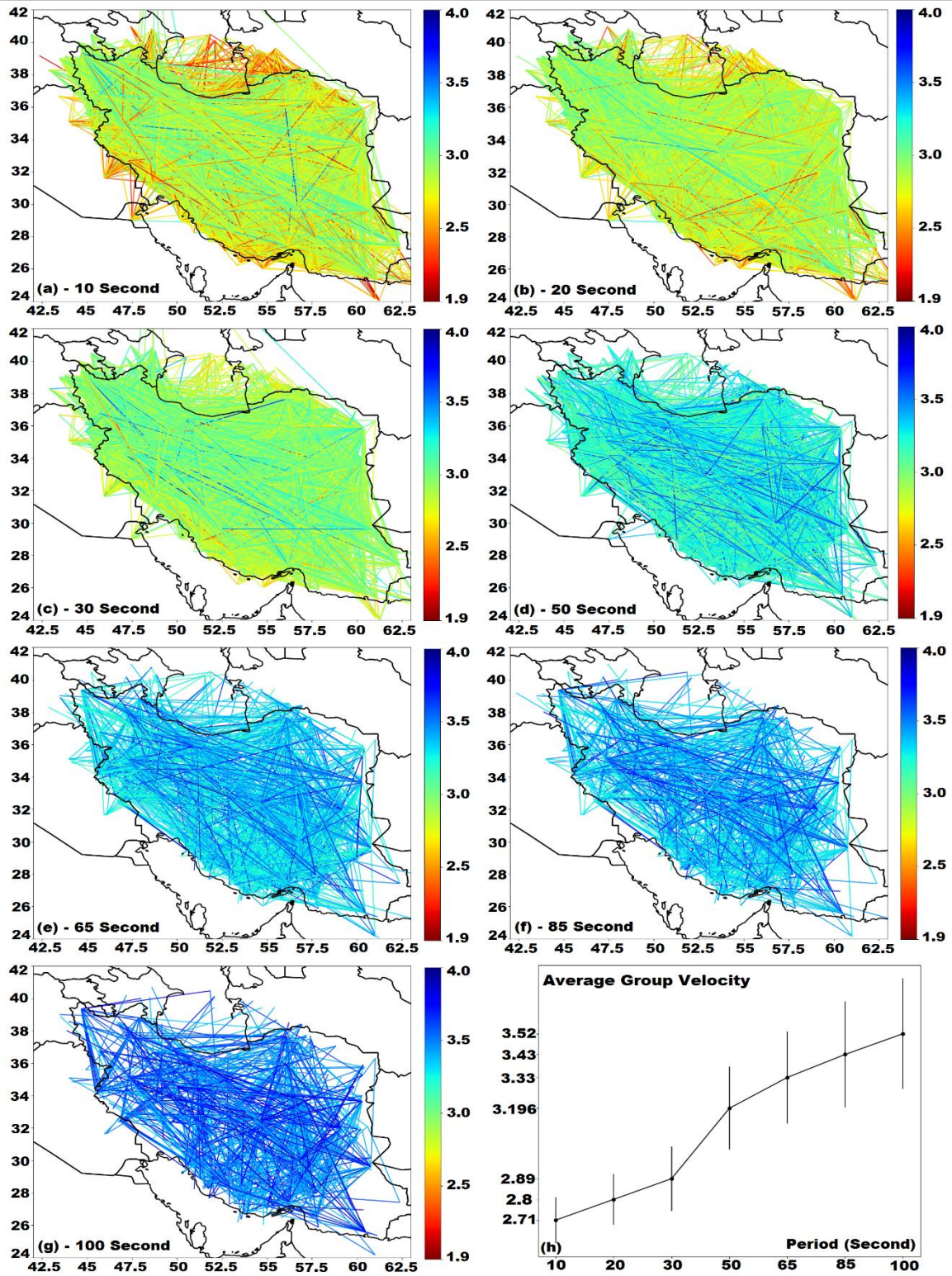
S1. Path coverage of group-velocity measurements at periods of 10, 20, 30, 50, 65, 85 and 50 s. Paths are colored by their respective group-velocity values. Graph shows the average group-velocities at each period; the error bars show the average uncertainties of the measurements at each period.
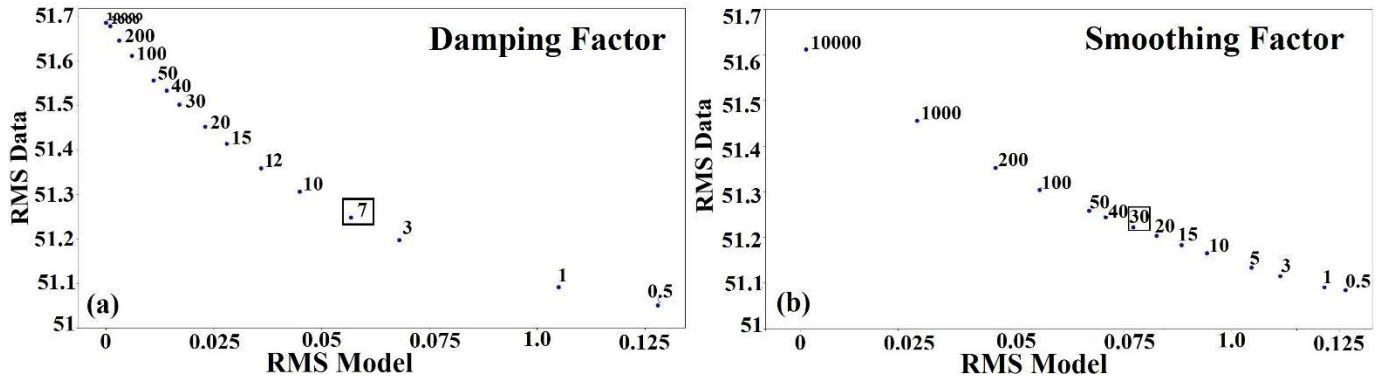
S2. Trade-off curves (L-curves) for Fast-marching (a,b) and SOLA inversions(c). A trade-off between data residual and model variance for different values of the damping (a) and smoothing (b) parameters for the Fast-marching Surface-wave Tomography method.
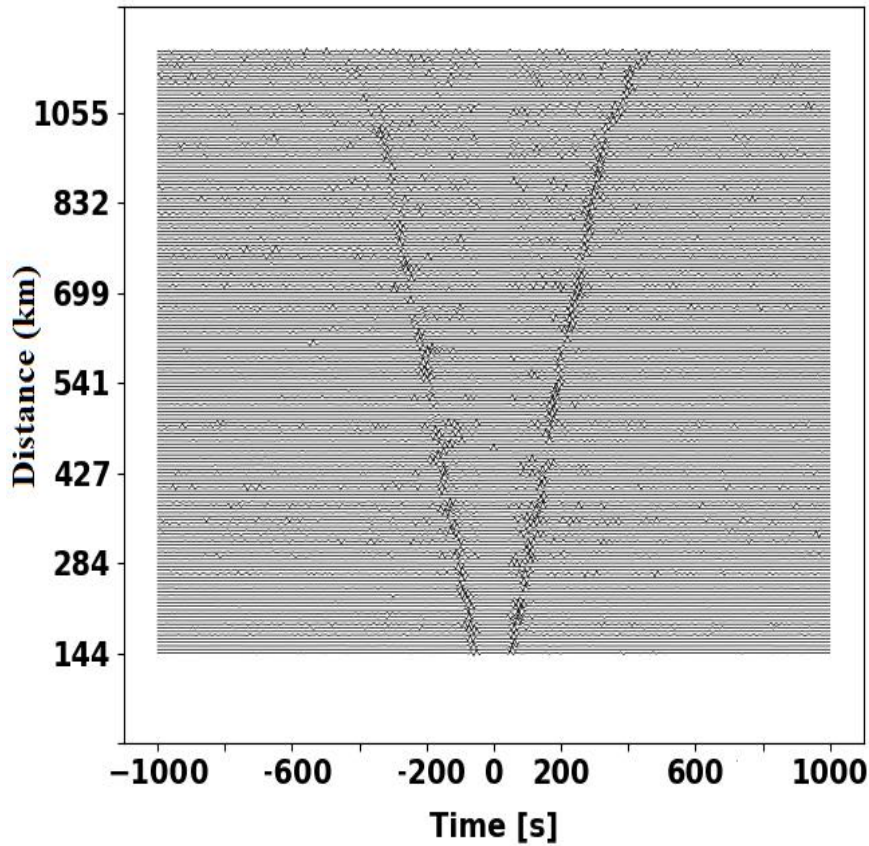
S3. Vertical two-sided noise correlation functions sorted by inter-station distance. The surface-wave move-out is between 2 and 4 km/s. Rayleigh-waves are observable at both positive (causal) and negative (acausal) lag times. Only the noise correlation functions with signal-to-noise ratios larger than 10 are plotted

Highlights

- New 3D Vs model of the Iranian Plateau from ambient noise and earthquake data

- SOLA Backus–Gilbert provides full resolution and spatially variable uncertainties

- Novel homogenization step ensures consistent resolution across all periods

- Bayesian MCMC inversion yields four Vs profiles with quantified uncertainties